

Solar Surfing

Final Report on a Phase I NASA Innovative Advanced Concepts Study

April 2018

**Robert C. Youngquist and Mark A. Nurge
Kennedy Space Center, NASA**

*Bruce Williams of the Johns Hopkins University Applied Physics Laboratory was a team member on our proposal but, due to contractual issues, was not able to participate in the Phase 1 effort.

Executive Summary

The Sun sustains life on Earth and NASA has made its study one of the four pillars of the Science Mission Directorate. A specific area of study, the coronal heating problem, has been of significant concern for nearly 80 years; namely how does the 5800 K surface of the Sun heat the nearby corona to over 1,000,000 K. Differing theories have been proposed to explain this process, but verification by actual measurement would not only resolve this issue, it would provide close-up measurements of the Sun never before obtained. However, this requires the development of a solar shield that can protect a satellite located less than 10,000 km from the Sun's surface. Steps towards that capability are the goal of this NIAC project.

The current state-of-the-art in solar shielding is best shown by the upcoming Parker Solar Probe Mission, so the approach taken by that satellite is discussed and used as a starting point; allowing a distance of 9.5 solar radii from the Sun's center to be reached. It is then shown that state-of-the-art solar reflectors do not improve this performance. Next, we review the use of pressed powder as a better solar reflector and show that there is some improvement, but not sufficient to reach the Sun's surface. We spend some time on this architecture because the Parker Solar Probe has a thin scattering layer on its solar shield and it is important to discuss the advantages and disadvantages of this feature.

A key concept that allows a spacecraft to come to within 1 Solar radii of the Sun's surface is to let the infrared radiation generated by the shield be emitted from the back side of the shield and then use a silvered plastic to reflect that infrared radiation away from the spacecraft. This allows the front of the solar shield to scatter away most of the Sun's power, i.e. low emissivity, while allowing the back side to emit most of the absorbed energy, i.e. high emissivity. But now another problem arises; up to this point the shield was assumed to be a flat sheet, however as the vehicle gets close to the Sun a flat shield is not sufficient to protect the spacecraft. A curved shield is needed to block the nearly 2π steradians of solar exposure and this curvature reduces the infrared emission from the back of the vehicle, causing a temperature rise. Modelling with a solar shield coated with BaF₂ shows that the nearest approach distance to the Sun's surface is about 0.6 Solar Radii before shield degradation, vehicle heat load, and the need for shield curvature all combine to prevent closer approach. However, through the use of possible new materials and a transient fly-by analysis the transition region might still be reached, but that analysis needs to wait for a future project.

As part of this NIAC project we developed relatively large (3-inch diameter) samples of our powder based solar reflectors. We had planned on sending these to the Johns Hopkins University Applied Physics Laboratory for high intensity radiative testing, but due to contractual issues this did not happen. However, in the development and aftermath of creating these large samples we significantly advanced the performance and attributes of our high reflectivity coating. In addition, we developed a connection with the Parker Solar Probe Team, which led to Mark Hasegawa, a thermal engineer at Goddard, becoming involved in the project. Dr. Hasegawa is sending a set of coatings to the International Space Station (ISS) for long term exposure testing and he gave up a spot so that our new coating could be included in this Low-Earth Orbit environmental test.

We have not achieved a design that can reach the surface of the Sun, but we have a design that should allow much closer approach than with the current state-of-the-art (by about a factor of 8). We also were not able to arrange for high irradiance testing, but instead have made substantial advance in the performance of our coating and we have a sample going to the International Space Station. Finally, JPL learned of this work and believe that it is potentially an enabling technology advance allowing future spacecraft to reach interstellar space in under 40 years by allowing the use of the Sun as a sling-shot.

We worked this Phase 1 NIAC project at the same time as a Phase 2 NIAC on a related topic, cryogenic selective surfaces. We have tried to separate the work, but some overlap inevitably occurs, especially in regard to

coating fabrication. Consequently, some of the experimental work described below, while performed under this NIAC because it was directly related to near Sun issues, may have impact and may be continued under our Phase 2 NIAC program.

Contents

1.	THE NEED TO REACH THE SUN’S SURFACE.....	3
2.	THE STATE-OF-THE-ART IN APPROACHING THE SUN.....	5
2.1	The Parker Solar Probe.....	5
2.2	The Use of Particle Based Coatings.....	7
2.3	Alternative State-of-the-Art Approaches.....	10
3.	CONCEPTS ALLOWING NEAR SUN APPROACH.....	11
3.1	More on Particle Coatings.....	11
3.2	Allowing Infrared Backward Emission.....	12
3.3	Temperature Dependence of the Shield Operation.....	15
3.4	Adding a Reflective Cone.....	16
3.5	Heat Flow Along the Struts.....	18
3.6	The Need for a Curved Shield.....	20
3.7	Additional Thoughts.....	22
3.7.1	Alternative Materials.....	22
3.7.2	Transient Thermal Response.....	23
3.7.3	Additional Shields.....	24
4.	EXPERIMENTAL WORK.....	24
4.1	High Irradiance Sample Preparation.....	24
4.2	Improved Coating Material.....	25
4.3	Reflectance Measurements.....	28
4.4	High Irradiance Testing and Water Issues.....	30
4.5	MISSE10.....	31
5.	FUTURE WORK AND CONCLUSIONS.....	32
5.1	New Mission Possibilities.....	32
5.2	Future Work.....	33
5.3	Conclusions.....	33
6.	REFERENCES.....	33
7.	APPENDIX I- MATERIALS COMPARISON FOR SOLAR SURFING.....	35
8.	APPENDIX II- A REPORT ON DETECTING AND REMOVING WATER FROM RIGID BAF2 SAMPLES.....	44
8.1	Introduction.....	44
8.2	Sample Preparation.....	44
8.3	Water Removal and Detection Methods.....	45
8.4	Other Water Removal Detection Methods.....	47
8.5	Results.....	47
8.6	Conclusions.....	49
8.7	References.....	50

1. THE NEED TO REACH THE SUN'S SURFACE

The Sun's irradiance is critical to life on Earth, providing the power to keep the planet warm and for vegetation to grow. But the Sun also emits a stream of charged particles, the solar wind, which impacts the Earth and can affect communications and satellite performance [1]. These charged particles have energies in the 1 keV range, corresponding to source temperatures of roughly 10,000,000 K. Yet, the surface of the Sun is at a temperature of roughly 5800 K and cannot be the source of these particles. Instead, these particles originate from the Sun's corona, a region above the surface of the Sun that extends out several solar radii and is at a temperature well above 1,000,000 K [2]. Which raises the question, "what heats the corona?"

There is a thin region above the surface of the Sun, called the transition zone, where the Sun transitions from a high density, 6000 K plasma dominated by gravity effects, to a tenuous, very hot plasma whose evolution is dominated by magnetic field effects. This thin region is only a few thousand kilometers in thickness [3], as shown in the plot in Figure 1-1. Also shown in Figure 1-1 is an image of the Sun with a blue circle whose thickness is scaled to show the average thickness of this transition region relative to the size of the Sun. So in passing through this thin layer the temperature rises by a factor of over 200 as the density drops significantly. This temperature rise is surprising in that it seemingly defies thermodynamics. Theories have been proposed to explain it, but none have yet been substantiated. This region is very difficult to model due to the need to combine Navier-Stokes with electrodynamics in a highly chaotic environment [3], so the resolution to this quandary will require observation and measurement, preferably taken from as close to the transition region as possible.

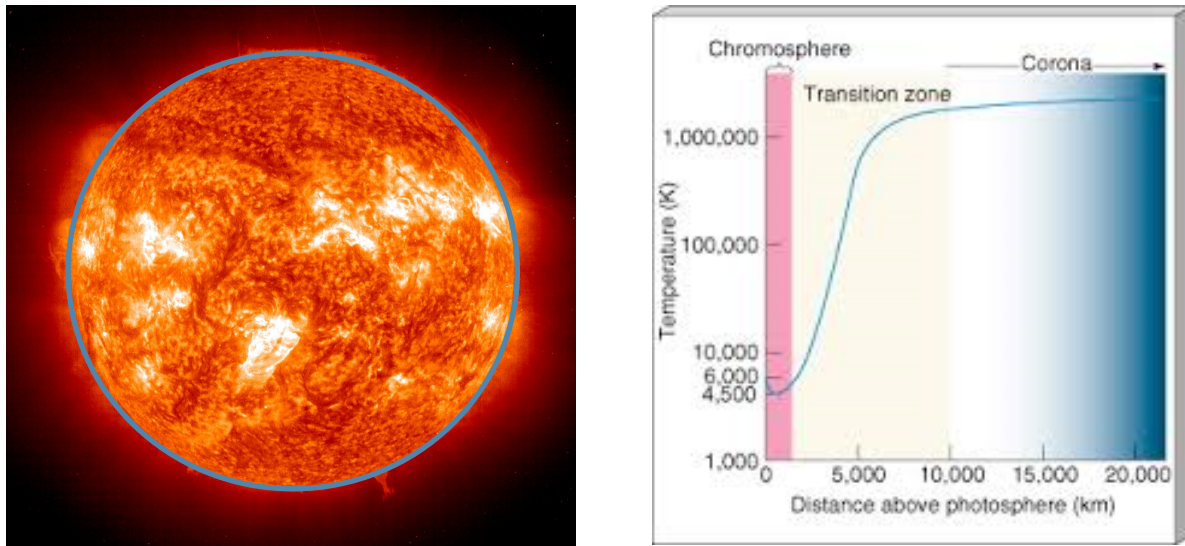


Figure 1-1. On the left is an image of the Sun where a blue circle indicates the average location and thickness of the Sun's transition zone and on the right is a plot of the temperature from the Sun's surface out to the corona (NASA images).

Several missions have been launched with the intent of studying the Sun's corona and helping to resolve the coronal heating problem. The first was the pair Helios-A and Helios-B which were launched in 1974 and 1976 respectively, with the intent of studying solar processes. These spacecraft came within 0.3 Astronomical Units (AU) of the Sun and carried a suite of scientific instruments to measure the magnetic field, the electromagnetic environment, plasma (charged ions), electrons, micro meteors, cosmic radiation, and other phenomenon [4]. Significant information was gained from these missions, but the coronal heating problem was not resolved. A later mission, the Transition Region and Coronal Explorer (TRACE) spacecraft, launched in 1998. TRACE was a telescope with passbands ranging from the far-ultraviolet to the visible, allowing imaging of plasma emission in the temperature range from 4000 K to 4,000,000 K [5]. The TRACE spacecraft, in orbit about the Earth, provided the first images of the Sun's transition region. (See the image in reference [3].) Numerous other solar study missions have been launched, but none have approached the Sun any closer than the Helios missions in the 1970s. A listing of these missions is available at https://science.nasa.gov/missions-page?field_division_tid=5&field_phase_tid=All showing all NASA Science Missions devoted to the Sun, including past, operational, and future.

Of significance to understanding the coronal heating problem are three future missions. The first is the Solar Orbiter, a joint European/NASA mission to approach within 0.3 AU of the Sun. While not approaching the Sun much closer than Helios, the Solar Orbiter will be in an orbit where it will stay positioned for several days over the same location of the Sun, allowing longer term monitoring of solar wind evolution, albeit from a significant distance [6]. The second is the Parker Solar Probe, which is planned to launch in 2018 and will approach the Sun to within 9.5 solar radii (less than 0.05 AU!). In much of this report we will use a solar radii as a unit of distance. One solar radii is about 700,000 km or 1/215 AU, i.e. the Earth is 215 solar radii from the Sun. We also state, from this point onward, solar approach distances as distances to the center of the Sun. For example, approaching the Sun to two solar radii would correspond to being one solar radii off of the Sun's surface [7]. The Parker Solar Probe represents the current state-of-the-art in solar shielding, approaching the Sun 6 times closer than Helios or the Solar Orbiter, and will be the starting point for our technical discussion in the next section of this report. The Parker Solar Probe will flyby Venus multiple times, losing angular momentum on each pass and allowing it to incrementally fall closer

and closer to the Sun. As this occurs it will enter the Sun's corona and take measurements of the magnetic field, particles, and radiation properties near the Sun with the intent of adding to our knowledge of the source of the solar wind. However, it will still be 8.5 solar radii from the transition region. The third future mission is the European Space Agency proposed PHOIBOS Spacecraft. The web site describing this mission was up in August 2017, but when this report was being written it was no longer operational. Even so, this spacecraft is being included because it is claimed that it can approach the Sun to within 4.5 solar radii. It does this by using a highly inclined solar shield (the Parker Solar Probe early design also had a cone shaped shield) allowing enhanced infrared emission. The benefits and problems associated with this approach will be discussed in the next section.

2. THE STATE-OF-THE-ART IN APPROACHING THE SUN

This section of the report will review the current state-of-the-art in solar shielding, using the Parker Solar Probe design as a starting point. A theoretical model of its solar shield will be developed that yields results consistent with the published performance for this mission. The key concern will be to prevent the spacecraft from overheating and the steps taken to achieve this will be discussed so that they can be compared to alternative approaches raised in the subsequent section. One feature of the Parker Solar Probe solar shield is a thin alumina scattering layer placed on the sun-side of the shield to reduce the absorption of the incoming sunlight. It is important to understand the pros and cons of this feature and special attention will be given to it, since it plays a much more important role in our proposed design than in the Parker Solar Probe. This section will end with a brief consideration of the use of available optical solar reflectors and highly inclined solar shields, showing their benefits and limitations.

2.1 The Parker Solar Probe

An artist's rendition of the Parker Solar Probe approaching the Sun is shown in Figure 2.1-1. The goal of this section is to develop a low-fidelity model of the operation of the solar shield used on this satellite so that its operation and limitations are understood. The model will only be low-fidelity for two reasons; it is not necessary to perform a detailed model to understand the basic operation of this shield and details of the shield's design and test data have been difficult to obtain. The authors have had communication with the Parker Solar Probe heat shield/thermal design team, but have chosen not to divulge that correspondence in this report. Instead, the shield design features presented here are taken from the published literature. In 2006 a thermal protection system risk mitigation study was released [8] and in 2010 a conference paper describing the shield coating was published [9]. Some details presented in these two references no longer apply to the current embodiment of the Parker Solar Probe, but the fundamental design features are sufficient to create a model of the shield's predicted performance.



Figure 2.1-1. The NASA released artist's conception of the Parker Solar Probe nearing the Sun.

For the purposes of this report we will model the Parker Solar Probe heat shield as being composed of 0.1 m of carbon foam (reticulated vitreous carbon) sandwiched between a carbon composite facesheet (carbon composite has an emissivity of about 0.9 over all of the solar wavelengths) facing the Sun and a back-sheet facing the spacecraft. The sheet facing the Sun has a thin layer of particulate alumina (Al_2O_3) placed on it to act as a solar reflector and gives the heat sheet a white color. The white alumina coating yields a facesheet emissivity of 0.54 [9]. We assume the alumina has properties similar to that of sapphire and that the facesheet emissivity is constant from the ultraviolet, through the visible, out to 5 microns wavelength. Beyond 5 microns we assume an emissivity of 0.9 because sapphire is black in this region, as is the underlying carbon composite. The carbon foam has a thermal conductivity of $0.14 \text{ W}/(\text{m}\cdot\text{K})$ [8] and the back-sheet facing the spacecraft has an emissivity of 0.8. The Parker Solar Probe is designed such that it can approach the Sun to within 9.5 solar radii of the Sun's center and the front of the heat shield will reach a maximum temperature of 1700 K.

The purpose of the carbon foam is to insulate the spacecraft from the high temperature of the front facesheet. Assuming the front facesheet reaches 1700 K and that the back-sheet faces away from the Sun—so there is minimal radiative heat load on it—then the temperature of the back-sheet is given by equating the heat flow through the carbon foam to the heat radiating from the back-sheet. Equation (1) shows this relationship where the carbon foam thermal conductivity multiplied by the temperature difference between the front facesheet and the back facesheet divided by the carbon foam thickness must equal the radiative heat given by the Stefan Boltzmann constant σ ($5.67 \times 10^{-8} \text{ W}/(\text{m}^2\text{K}^4)$) times the back-sheet emissivity, ε (assumed to be 0.8), times the back-sheet temperature raised to the fourth power.

$$0.14\text{W}/(\text{mgK})(1700 - T) / (0.1 \text{ m}) = \sigma\varepsilon T^4 \quad (1)$$

Solving this equation yields a temperature of 445 K for the back facesheet, indicating that about $1800 \text{ W}/\text{m}^2$ power density flows through the carbon foam and is emitted by the back of the shield. However, the total energy radiated

by the shield in the forward direction is more than 420,000 W/m², indicating that the carbon foam is effective at protecting the spacecraft; essentially all of the absorbed solar power is radiated from the forward facesheet back towards the Sun.

The Sun's total irradiance at the Earth, 1 AU or 215 solar radii from the Sun, is 1377 W/m². Since energy cannot be stored in space, the total wattage flowing through any closed surface containing the Sun must have the same total power flowing through it. Assuming the Sun's irradiance is uniform, this implies that the Sun's irradiance at a distance R from the Sun is given by $1377 (215/R)^2$ W/m², where R is in units of solar radii, i.e. a standard one-over-R-squared dependence. So assume for the moment that the alumina is removed from the front face of the Parker Solar Probe heat shield. In this case the front facesheet has a wavelength independent emissivity of 0.9. Assuming the front facesheet can reach 1700K, the minimum allowable distance to the Sun can be calculated by equating absorbed solar power to thermally radiated power. The absorbed power is the emissivity times the solar irradiance and the thermally radiated power is given by the Stefan Boltzmann constant times the emissivity times the temperature, 1700K, raised to the fourth power.

$$(0.9)(1377\text{W/m}^2)\left(\frac{215}{R}\right)^2 = \sigma(0.9)(1700)^4 \quad (2)$$

Solving this yields a minimum distance to the center of the Sun of 11.5 solar radii. If we allow the shield to reach 1900K then the probe can approach the Sun to within 9.3 solar radii without the Al₂O₃ layer.

Now consider the alumina, Al₂O₃, layer used on the sunward side of the Parker Solar Probe heat shield. One reason for this layer is that it is white in the visible region of the spectrum, indicating that it scatters visible light corresponding to the peak spectral intensity of the Sun. So one might assume that Equation (2) can be simply modified to reduce the absorbed solar power by the emissivity of this white layer, i.e. changing the 0.9 on the left side of Equation (2) to a 0.54. Doing this yields a nearest solar approach distance of 9 solar radii, closer than the design distance of 9.5 solar radii. However, this approach is overly simplistic as will be developed in the next section. The problem is that the Al₂O₃ layer scatters wavelengths out to 5 microns and a 1700 K object emits its peak thermal energy (Wien's Law) at 1.7 microns, which is less than 5 microns. So the underlying carbon composite facesheet cannot radiate with an emissivity of 0.9. It has reduced average emissivity and as a consequence is at a higher temperature. Calculations show that this increase is almost 200 K, i.e. the alumina layer has minimal impact on the facesheet temperature because it reduces the solar absorption by roughly the same factor as it reduces the ability of the front facesheet to thermally radiate. This issue was brought to the attention of the Parker Solar Probe thermal team who arranged a telecom to discuss it. They pointed out that the analysis shown above is approximate and that the shield can survive temperatures above 1900 K. So using 1900 K as the shield temperature the Parker Solar Probe, with the Al₂O₃ coating performing as described above, can approach the Sun to within 9 solar radii.

2.2 The Use of Particle Based Coatings

The reason for studying the Parker Solar Probe is to become acquainted with the state-of-the-art in solar heat shields, however, while analyzing this heat shield we realized that its performance could have been improved by applying a thicker particle-based alumina coating. Since this insight is important to understanding our proposed improvements to Sun shield performance some development of it is warranted.

It is well-known that particle based scattering can be used to create a white surface and that this is the basis of white paints where particles composed of non-absorbing materials are held in place by a transparent binder, i.e. a glue [10]. Visible light entering the paint is not absorbed by the particles, nor the binder, and instead is scattered, such that a significant portion of the light is reflected by the coating. A wide variety of such white coatings have been evaluated and are available for use in space [11, 12] where they provide reflectance of the visible portion of the

Sun’s power spectrum. The problem with most of these coatings is that the binders often absorb ultraviolet radiation, limiting their performance. The optics community had a similar problem and solved it in the 1960s [13] by developing pressed powder coatings, i.e. coatings composed of only particles with no binders. Doing this removed the binder absorption and allowed the use of very wide transmission band materials. Also, by optimizing the particle size and using sufficiently thick coatings nearly perfect reflectance could be achieved (see [14] for Kubelka Munk’s original paper on the optical theory of paint). So by choosing an appropriate material to compose the scattering particles, a coating could be demonstrated with very high reflectance across a very wide band of radiation.

This insight, as applied to achieving cryogenic temperatures at 1 AU from the Sun, was the basis for our previous NIAC Phase 1 study entitled “Cryogenic Selective Surfaces” [15, 16]. In that work we developed a sophisticated model predicting the reflectance of a thick particle based scattering layer on top of a metallic (typically silver) layer. In addition, by considering the absorptive regions of the coating material, we predicted the long wave infrared absorptivity of the coating. Kirchoff’s law of thermal radiation states [17], “For an arbitrary body emitting and absorbing thermal radiation in thermodynamic equilibrium, the emissivity is equal to the absorptivity”. Using this, the absorptivity results from our model are equal to the emissivity, $\epsilon[\lambda]$, of the coating as a function of wavelength.

Now consider a plate with a wavelength-dependent emissivity, $\epsilon[\lambda]$, facing the Sun, that is coated with a layer of particles where minimal power migrates through the plate. In this case we can equate the absorbed power to the thermally radiated power yielding

$$\int_0^{\infty} I_s[\lambda]\epsilon[\lambda]d\lambda = \frac{2\pi hc^2}{\lambda^5} \int_0^{\infty} \frac{\epsilon[\lambda]}{\exp[\frac{hc}{\lambda kT}]-1} d\lambda \quad (3)$$

where $I_s[\lambda]$ is the solar irradiance spectral density, h is Planck's constant, c is the speed of light, and k is the Boltzmann constant. In other words, the total absorbed solar radiation is obtained by integrating the Sun's irradiance at each wavelength times the absorption of the plate at each wavelength. The total thermal power emitted is obtained by integrating the plate emission at each wavelength times the Planck Blackbody radiation law. Equating these yields an expression where the resulting equilibrium temperature of the plate can be found (though this requires the use of a numerical algorithm which we programmed in Mathematica). Note that if the emissivity, $\epsilon[\lambda]$, is equal to one for all wavelengths then the surface is called a blackbody. If it is equal to some constant between 0 and 1 for all wavelengths then the surface is called a grey body and Equation (3) reduces to Equation (2). If the emissivity varies with wavelength, particularly if it has very different values in the visible than in the infrared, then the surface may be referred to as a selective surface or a thermal control coating. Finally, if a surface has perfect reflectance, i.e. 0 emissivity, from the short wave ultraviolet to some wavelength and then transitions to a perfect emitter, i.e. emissivity of 1, from that wavelength out to very long wavelengths, then we call the surface a Hibbard Ideal Selective Surface in honor of Hibbard who first analyzed this [18].

Now we have the tools to study the Al_2O_3 coating on the Parker Solar Probe heat shield. We can start by letting the emissivity equal 0.54 from the ultraviolet to 5 microns and 0.9 from 5 microns to the far infrared. Substituting this into Equation (3) yields a temperature of 1900 K when the satellite is 9 solar radii from the Sun. This provides more detail into the analysis in the prior section, but now we can also assess the use of thicker layers of alumina. As mentioned above, by making the alumina layer thicker, it also becomes whiter, i.e. a better reflector, in the UV to 5-micron spectral band. Figure 2.2-1 shows the temperature effect on the shield resulting from different reflectance values ranging from 0.1 to 0.9. Using a thick coating and correspondingly high reflectance (i.e. 0.1 emissivity) drops the shield temperature to 1600 K at 9 AU and would allow the vehicle to approach to less than 8 AU from the Sun. Optimizing the use of a highly reflective coating composed of scattering particles will be the first topic addressed in Section 3 where we move beyond the state-of-the-art.

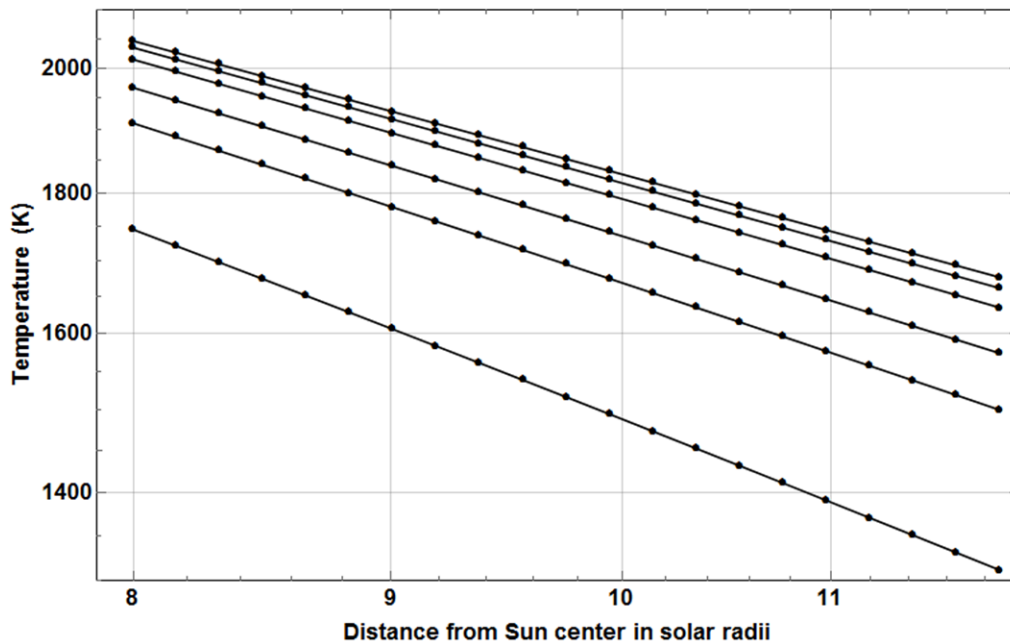


Figure 2.2-1. Predicted heat shield temperatures with the emissivity beyond 5 microns equal to 0.9 and the emissivity less than 5 microns set to 0.1, 0.2, 0.3, 0.5, 0.7, and 0.9 in order from lowest plot to highest plot.

2.3 Alternative State-of-the-Art Approaches

There are two other state-of-the-art approaches that are deserving of mention, the use of a tapered heat shield and the use of second surface mirrors.

The PHILOBOS Spacecraft is advertised as being able to approach to within 3.5 solar radii of the Sun's surface (4.5 solar radii from the Sun's center). This is possible because its conical shield has a larger emission area from which heat can be radiated than its solar absorption cross section. If the cone half angle is α then the emission area is increased by a factor of $1/\sin\alpha$. For example, if we assume a carbon composite shield with no coating (i.e. the emissivity is wavelength independent) that can reach 1900 K, then the minimum distance to the Sun is obtained by multiplying the right hand side of Equation.(2) by $1/\sin\alpha$, i.e.

$$(0.9)(1377\text{W/m}^2)\left(\frac{215}{R}\right)^2 = \sigma(0.9)(1900)^4 / \sin\alpha \quad (4)$$

The half angle might be as small as 15 degrees in which case the minimum approach distance to the Sun becomes 4.7 solar radii, which is very close to the advertised 4.5 solar radii.

This approach does succeed in reducing the Sun's approach distance, but relies on increasing the shield emission area while not increasing the solar absorption. The difficulty is that at 4.5 solar radii the Sun fills approximately 26 degrees of the sky and the shield has to block radiation coming in from a wide angular source. So the solar absorption area is increased and the left hand side of Equation (4) should account for this. We will not develop that analysis, but the net result is that this idea, of using a cone instead of a plate as a solar shield, allows closer solar approach, but fails when the Sun fills a substantial region of the field of view.

The other state-of-the-art approach is to consider the use of optical solar reflectors. These are typically thin quartz windows with a layer of silver on the backside. The Sun's radiation passes through the quartz and reflects off of the silver, yet the quartz is absorbing beyond 3 microns and acts as an efficient long wave radiator. These are available as space rated items [19]. However, silver absorbs substantial short wave solar radiation (about 6% of the Sun's total irradiance) and quartz absorbs about 2 percent of the Sun's irradiance in the region above 3 microns. So the temperature of a state-of-the-art optical solar reflector is given by a slightly modified version of Equation (2), where 8 percent of the Sun's total irradiance is absorbed, but the surface can still emit efficiently.

$$(0.08)(1377\text{W/m}^2)\left(\frac{215}{R}\right)^2 = \sigma(0.9)(T)^4 \quad (5)$$

The limiting effect is the relatively low melting point of silver, (1235 K), yielding a minimal approach distance to the Sun of 6.5 solar radii. However, operating right at the melting point is dangerous. If we drop back to 1000 K the minimal approach distance is about 10 solar radii, not much different from the Parker Solar probe result.

This section has shown that the Parker Solar Probe, representing the state-of-the-art, can approach the Sun to within 9 solar radii of its center, but that modifications are possible that could be used to reduce this approach distance. A white particle layer can reduce the solar absorptance and a conical or hemispherical shape could increase the emittance to absorptance areas. In the next section these and other modifications will be discussed with the goal of minimizing the approach distance to the Sun.

3. CONCEPTS ALLOWING NEAR SUN APPROACH

3.1 More on Particle Coatings

As shown above, by increasing the thickness of the Al_2O_3 coating on the Parker Solar Probe, substantially less solar radiation is absorbed and the solar approach distance is reduced. Adding such a highly reflective coating to a solar shield can greatly reduce the absorbed power and subsequent high temperatures, so this section of the report continues to develop the use of particle based coatings.

Under our Phase 1 NIAC entitled “Cryogenic Selective Surfaces” [15, 16] we developed a detailed model of a coating composed of scattering particles on top of a reflective layer that yielded the emissivity as a function of wavelength. We have been using that model to make predictions of shield temperature as a function of solar distance, but before showing those results, a simpler case will be considered in order to demonstrate an issue with the use of particle scattering coatings. Assume four different solar shields; one is a blackbody with no dependence of emissivity on wavelength. The other three have an emissivity of 0.001 below a cutoff wavelength and unit 1 emissivity above that wavelength and have cut-off wavelengths of 5 microns (e.g. Al_2O_3 -sapphire), 13 microns (e.g. BaF_2 -Barium Fluoride), and 30 microns (e.g. KBr -Potassium Bromide). All of these coatings are placed on a thick layer of insulative material causing essentially all of the absorbed solar power to be remitted as long wavelength thermal radiation back towards the Sun.

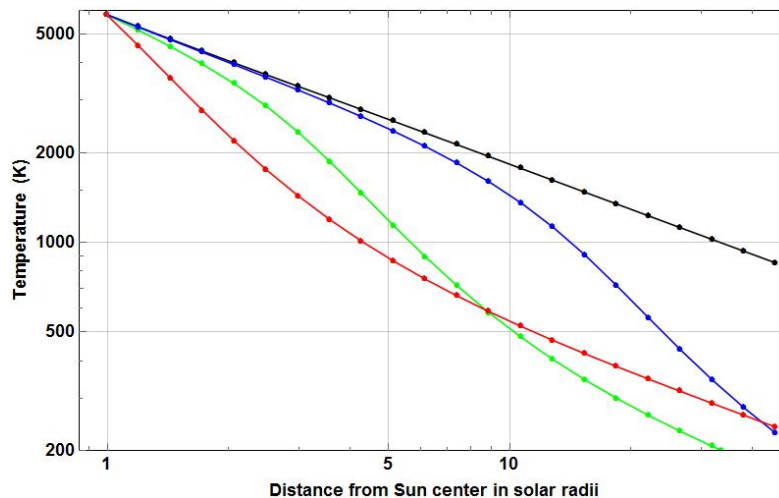


Figure 3.1-1. Predicted heat shield temperatures for emissivity equal to 0.001 below a cutoff wavelength and equal to 1 above that wavelength as a function of distance to the Sun. The black curve is a blackbody, blue has a 30 micron cutoff, green has a 13 micron cutoff and red has a 5 microns cutoff.

Using Equation (3) the temperature of these shields as a function of the distance to the Sun’s center can be found and the results are shown in Figure 3.1-1. The blackbody result on this log-log plot is a straight line as expected from the polynomial relationship indicated in Equation.(2). The interesting point is that all of the coated shields yield much lower temperatures than the blackbody shield when far from the Sun, but all three approach the same temperature as the blackbody shield as the solar distance becomes small. This result is due to the same principal as described above for the Parker Solar Probe. At long distances from the Sun the shield is cold and can emit thermal radiation, but as the shield approaches the Sun and gets hot, its emission band moves into the low emissivity region and the shield cannot effectively radiate energy. Consequently, the shield gets hot quickly upon further reduction in the Sun distance and ends up reaching the same temperature as a blackbody. Surprisingly, even though materials with minimal solar absorption, like BaF_2 and KBr , yield cold (even cryogenic) temperatures at 1

AU from the Sun, they yield temperatures higher than sapphire when the shield is 6 solar radii from the Sun. So the use of these novel particle scatters alone does not improve the performance of the solar shield and a modification to the design is required.

3.2 Allowing Infrared Backward Emission

The purpose of the carbon foam insulation used in the Parker Solar Probe is to minimize infrared emission toward the spacecraft (see the discussion around Equation (1)), but consider what would happen if this insulation was removed allowing the solar shield to emit in both the forward as well as the backward directions. Using the Parker Solar Probe emissivity values Equation (2) above becomes

$$(0.54)(1377\text{W/m}^2)\left(\frac{215}{R}\right)^2 = \sigma(0.9)(T)^4 + \sigma(0.9)(T)^4 \quad (6)$$

In this case, the power absorbed from the Sun (left hand side) is equal to the power emitted from the front of the shield plus an identical amount of emitted power from the back of the shield. Setting the Sun distance to 9 solar radii, which previously yielded a temperature of 1700 K, now yields a temperature of 1400 K. Recall that this is an approximate result because the alumina coating on the front of the shield inhibits the emission of some radiation, but it shows the need for the foam insulation. Without the insulation the shield would emit at least $\sigma(0.9)(1400)^4 \approx 200,000\text{W/m}^2$ of infrared power onto the nearby payload, essentially cooking it.

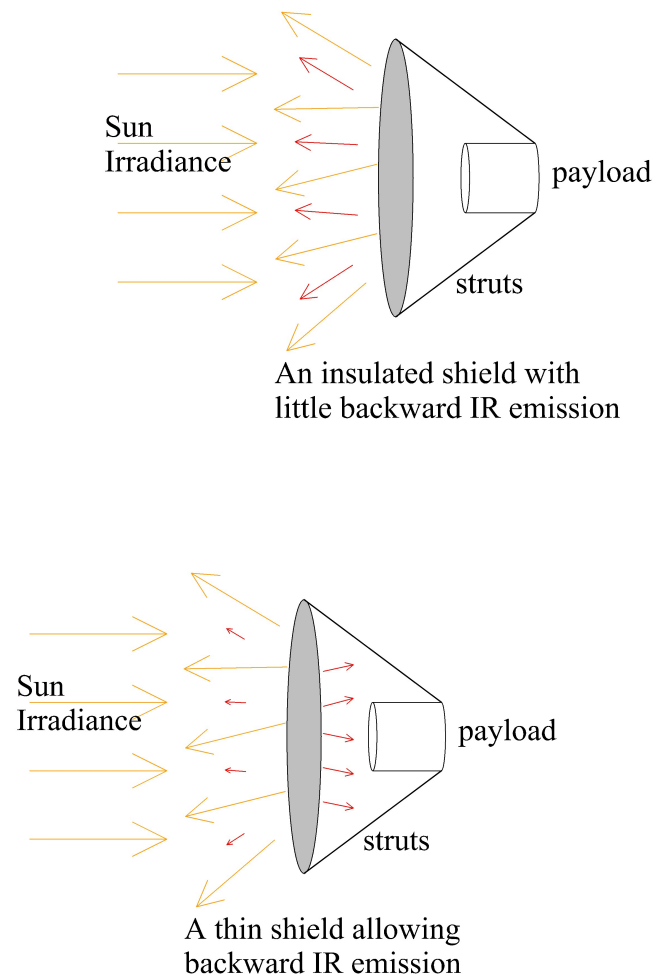


Figure 3.2-1. The left sketch shows a strawman design for a Solar spacecraft with an insulative shield that minimizes heat flow, resulting in infrared emission in the sun direction, but minimal IR emitted toward the payload. The right sketch shows a strawman design where the insulation is removed allowing heat to be emitted toward the spacecraft.

But consider the case of a coated shield designed to absorb only 0.1% of the Sun's energy, so the 0.54 factor in Equation (6) is replaced by 0.001. The temperature of the shield then drops to 300 K, the same temperature as the payload. Using a highly reflective surface and allowing infrared radiation to be emitted from the back of the shield significantly lowers the temperature of the shield and puts minimal infrared load onto the payload. Figure 3.2-1 shows the two cases; a shield that absorbs roughly half of the Sun's irradiant power and then reemits it as longwave shifted radiation and a shield that scatters most of the Sun's irradiant power and emits a substantial portion of the absorbed power backwards at the payload.

As described above, Equation (6) only approximates the temperature of the shield. Using a more detailed model, as described in reference [16], we can model a shield coated with a thick layer of fine Barium Fluoride (BaF_2) particles. Barium Fluoride has a broad spectral transmission, 0.14 microns to 13 microns (see Figure I-2, Appendix I). During our prior work we developed a process by which BaF_2 powder could be turned into a rigid

structure. The powder is mixed with water, pressed into a mold, and then sintered in an oven. Figure 3.2-2 shows a picture of a BaF_2 rigid sample along with a scanning electron microscope (SEM) image of the particle structure on the surface of this sample.

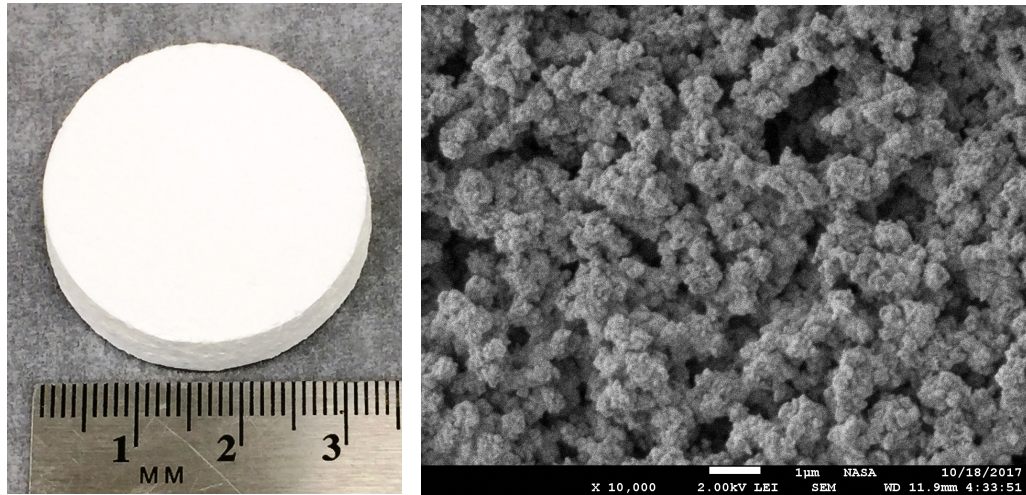


Figure 3.2-2. To the left is a rigid BaF_2 disk composed of BaF_2 particles. The particle nature is shown in the SEM image on the right.

A detailed theoretical model was developed under our prior work that predicted the solar absorption and infrared emission of a BaF_2 particle based coating as a function of wavelength. Note that in our prior work we assumed a silver layer on the backside of the BaF_2 particle layer whose purpose was to enhance the reflection of long wave radiation that partially propagated through the BaF_2 particles. The results shown below assume that this very thin silver layer is present. Having said that, the model then allows the temperature of a solar shield composed of a BaF_2 front surface and a black emitting back surface to be predicted. The orange curve in Figure 3.2-3 shows the results of running this model for a 3 cm thick layer of BaF_2 . This more detailed analysis shows that at 9 solar radii the shield temperature is below 300K! Restating this, the 1900K solar shield temperature predicted for the Parker Solar Probe at 9 solar radii from the Sun's center, is reduced to below 300 K by adding a layer of BaF_2 particles to the front of the Sun shield and allowing infrared emission from the backside. This dramatic drop in temperature is achieved by the use of a coating that absorbs only 0.1% of the Sun's energy instead of 54% and then allows most of the generated heat to be radiated away by a high emissivity coating on the backside of the shield.

As an aside, Table 1 in the first appendix shows that the temperature at the surface of the sun is essentially the same for a 1 cm thick layer as for a 7 cm thick layer of BaF_2 , both of which are the same as for the 3 cm case shown below. In other words, there is minimal gain in performance of the coating with thicknesses greater than 1 cm.

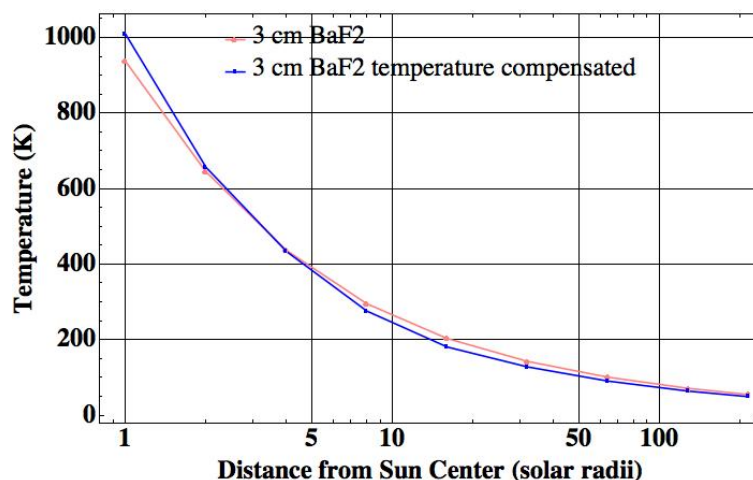


Figure 3.2-3. This plot shows the temperature of a flat solar shield with a 3 cm thick layer of BaF₂ particles on the solar side and a high emissivity emitting coating on the back side as a function of distance to the Sun.

3.3 Temperature Dependence of the Shield Operation

Our previous models were developed for cryogenic temperature operation and we used optical constants from [20] which were measured at 300 K. As can be seen in Figure 3.2-3, the shield temperature may be substantially higher than 300 K as the Sun is approached. BaF₂ melts at 1641 K but our sintering process occurs at about 1050 K. In order to prevent the shield from further sintering we will adopt a maximum temperature for the BaF₂ coating of 800 K.

The optical constants of materials can change with temperature and we were concerned that this would alter the optical properties of the broadband spectroscopic materials as they approached the Sun, so we devoted a significant amount of effort to trying to obtain the optical constants of various materials over a wide temperature range. Our first literature searches did not provide much information of use; a few of the more appropriate ones are listed in the references [21, 22, 23, 24]. Then we located a pair of conference publications that looked promising [25, 26] in that they claimed to have models of the optical properties of materials as a function of temperature. These papers referenced a thesis that appeared to be helpful, so we made arrangements to have this copied and shipped to us [27]. Sadly, it did not provide much useful information. Then, we located a paper [28] that did provide the complex index of refraction of BaF₂ as a function of temperature and we were able to incorporate this into our models.

It should be noted that broadband spectroscopic materials typically have a transmission cutoff in the ultraviolet where high energy radiation can cause an orbiting electron to change energy state. Changing the temperature of the material to the melting point should have little or no effect on this absorption band. However, at long wavelengths these materials terminate their transmission band when the incoming radiation can excite vibrational bands in the material lattice. This absorption is temperature dependent because heating also excites vibrational bands allowing the incoming radiation to more easily access higher level vibrational states. So at low temperature the absorption spectrum of a typical broadband transmission material has a moderately sharp, i.e. somewhat narrow but high, absorption at some wavelength. As the material is heated the peak absorption drops, but also widens, allowing a broader range of incoming frequencies to be absorbed by the material.

Incorporating the temperature dependent optical parameter information from [28] into our BaF₂ model we were able to predict the temperature of our solar shield as a function of distance to the Sun and this result is shown in blue in Figure 3.2-3. Note that the differences between using the 300 K values and the temperature compensated values are minor until the shield reaches a temperature above 600 K. However, even at the surface of the Sun, the

difference in predicted shield temperatures is only about 70 K. The effect is relatively minor because the material temperatures are still far from the melting point for BaF₂, so the optical parameters of the BaF₂ do not vary significantly. Based on this result and on the difficulty in locating temperature dependent optical coefficients, we decided to use the published 300 K optical values for our models noting that this may not be accurate if the predicted temperatures become a substantial fraction of the melting temperature.

3.4 Adding a Reflective Cone

As shown above, allowing backward infrared emission reduces the solar shield temperature, but, as highlighted by the Parker Solar Probe case, can result in projecting excessive heat onto the payload. Even if we use a BaF₂ coating to minimize the absorption of solar irradiance, as the spacecraft approaches the Sun, the shield temperature can become high enough that the payload is overheated. Assume for the moment that the side of the payload facing the solar shield has an emissivity of 0.2 (metallic), that the payload is operating at $T_{payload} = 300\text{K}$, that the shield nearly fills the field of view of the payload, and that the payload cannot tolerate more than 100 Watts/m² of excess heating, then the following expression yields the maximum shield temperature, T_{shield} .

$$(0.2)(0.9)\sigma T_{shield}^4 - (0.2)\sigma T_{payload}^4 < 100\text{W/m}^2 \quad (7)$$

This states that 20% of the shield power density emitted towards the payload is absorbed by the payload and that the payload emits thermal power with a 20% emissivity. Solving this yields a maximum shield temperature of 370 K. Looking at Figure 3.4-1, this corresponds to a minimum solar approach distance of about 5 solar radii. While this is impressive, a relatively simple modification provides a substantial improvement. Replace the payload emissivity in Equation (7) with a variable given by ϵ_p . Now solve Equation (7) for the shield temperature yielding

$$T_{shield} < \left(\frac{100\text{W/m}^2}{0.9\epsilon_p\sigma} + \frac{T_{payload}^4}{0.9} \right)^{1/4} \quad (8)$$

This shows that the allowable shield temperature is determined by two terms, one related to the temperature of the payload, which is fixed, and the other related to the amount of energy absorbed by the payload, which can be varied by changing the payload emissivity. For example, if the payload emissivity is similar to that of silver, say 0.02, then the shield temperature can rise to 570 K, about 2.6 solar radii from the Sun's center as seen in Figure 3.4-1.

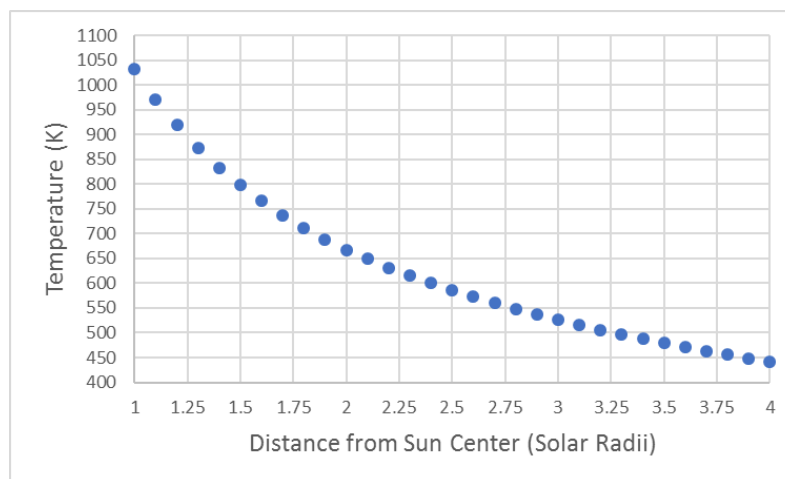
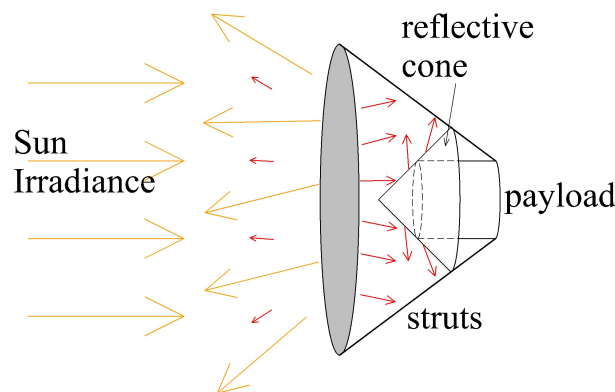


Figure 3.4-1. This plot shows the temperature of a flat solar shield with a 1 cm thick layer of BaF₂ particles on the solar side and a high emissivity coating on the back side as a function of distance to the Sun (temperature compensated optical data).

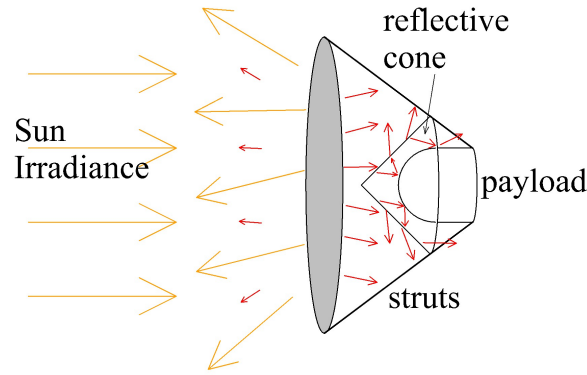
However, if the payload is coated with silver on the side facing the shield then the infrared energy coming from the shield will be reflected back at the shield and increase the shield temperature. So in order to prevent this increase in the shield temperature a reflective cone can be placed between the shield and the payload as shown in Figure 3.4-2. This cone is shaped such that essentially all of the infrared emission from the solar shield that hits the reflective cone is reflected to the sides of the spacecraft and not back at the shield. The back of the cone is assumed to have high emissivity, e.g. 0.9, allowing it to emit radiation backward into space and also towards the payload. We assume that the cone is primarily supported by the struts and is thin, but adequately rigid that it can be supported by its edges. For example, it could be composed of a thin sheet of graphite or carbon fiber coated with a protected silver layer.

This cone design shown in Figure 3.4-2, with an assumed secondary shield emissivity of 0.02, will allow the payload to approach to within 2.3 solar radii of the Sun. But this assumes that the payload and the cone are at the same temperature. We can gain more performance by decoupling the payload from the cone as shown in Figure 3.4-3 so that they are at different temperatures. As before, we assume the payload cannot tolerate more than 100 W/m² of excess heat, but we assume that the payload has an emissivity of 0.2 (metallic) so that it only absorbs 20% of the cone's IR emission. However, this also means that 80% of the infrared radiation hitting the payload is reflected, some of which returns to the cone, heating it. We assume that, on average, half of this reflected 80% returns to the cone and the other 50% is emitted into space.



A thin shield allowing backward IR emission and a reflecting cone.

Figure 3.4-2. A strawman design for a Solar Spacecraft where heat is emitted backward from the shield and then reflected by a reflective cone to protect the payload.



A thin shield allowing backward IR emission, a reflecting cone, and a reflective payload coating.

Figure 3.4-3. A strawman design for a Solar Spacecraft where heat is emitted backward from the shield and then reflected by a reflective cone to protect the payload and where the payload is decoupled from the cone, allowing some of the cone's IR emission to be reflected into space.

To analyze this, start with Equation (7), but now the payload sees the infrared emission from the cone, not the solar shield.

$$(0.2)(0.9)\sigma T_{cone}^4 - (0.2)\sigma T_{payload}^4 < 100\text{W/m}^2 \quad (9)$$

Where the cone temperature is found by equating its absorbed power to its emitted power. The equation below states that the solar shield emits substantial infrared power at the cone, but the cone only absorbs 0.02 of this. The payload emits much less power, but because the cone is black on its backside it absorbs 0.9 of that energy. The cone can then radiate a small amount of power back towards the solar shield, but most of its emission is towards the payload. Some of the cone emission towards the payload is reflected back at the cone where it is reabsorbed (the third term on the left side of the equation)

$$\sigma(0.9)(0.02)T_{shield}^4 + \sigma(0.9)(0.2)T_{payload}^4 + \sigma(0.9)(0.8)(0.5)T_{cone}^4 = \sigma(0.02)T_{cone}^4 + \sigma(0.9)T_{cone}^4 \quad (10)$$

Equation (9) can be solved for the maximum temperature of the cone (recall that the payload is assumed to be at 300 K), yielding a cone temperature of 370 K. Then putting this into Equation (10) yields a solar shield temperature of 840 K (slightly higher than our conservative maximum temperature to prevent sintering). Looking at Figure 3.4-1, this implies that we can approach the Sun to about 1.4 solar radii (less than 1/2 a solar radii from the surface)!

However, at such a close distance a flat shield cannot block the Sun from hitting the payload. Before considering that though, another issue will be addressed, namely heat flow along the support struts.

3.5 Heat Flow along the Struts

In Figure 3.5-1 a strawman design for the solar probe is shown with some selected dimensions, based on the availability of a launch vehicle that could accommodate a 4 meter diameter solar shield. The payload is assumed to

be 1 meter in diameter with the front edge located 1 meter from the solar shield. The cone is between the payload and the solar shield, not touching either. The key structural elements are the struts which connect the edges of the solar shield to the edges of the cone to the back edge of the payload. With the dimensions shown the struts are 2.5 m long.

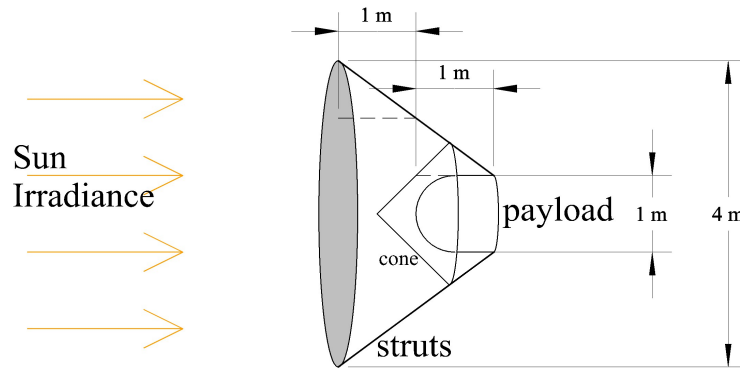


Figure 3.5-1. The Solar Probe strawman design with selected dimensions added.

The goal of this section is to estimate the amount of heat that propagates along the struts from the hot solar shield end to the vehicle end. We assume that:

1. The struts do not see the Sun; they are shielded by the Sun shield and by the reflective cone.
2. The struts are 2.5 meter long titanium tubes with an outer radius of 0.1 meter and wall thickness of 3 mm.
3. The inner half side of the struts, i.e. the side facing the solar shield and vehicle is coated with silver yielding an emissivity of 0.02.
4. The outer half side of the struts, i.e. the side facing away from the solar shield and vehicle, is coated black with an emissivity of 0.9.
5. The end of the strut attached to the solar shield is at 840 K and the end attached to the vehicle is at 300 K.
6. The thermal conductivity of titanium ranges from 6.8 W/(m·K) at 273 K to 19 W/(m·K) at 1073 K [30]. We use these two data points as well as 12.5 W/(m·K) at 473 K and 16 w/(m·K) at 863 K, to provide four points for interpolation of the thermal conductivity of titanium as a function of temperature.

Using these assumptions, a temperature profile along the strut can be obtained numerically. The strut is decomposed into 250 equal length segments (1 cm long each). Each segment has power flowing into it or out of it by conduction with the adjacent segments on either side. The silver side of the strut segment sees the solar shield and absorbs 0.02 of the radiant thermal power falling on it from the shield. In order to be conservative we assume the strut's field of view is filled by the solar shield. The strut segment can also radiate thermal energy on its silver side and on its black side. Note that the radiant emission area is proportional to the outside area of the round strut while the energy absorbed is proportional to the cross sectional area of the strut.

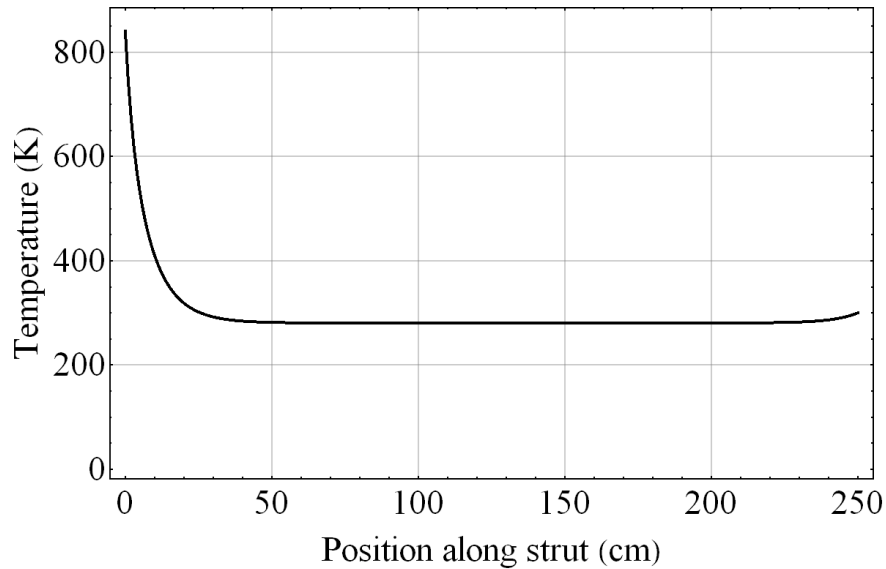


Figure 3.5-2. The temperature profile along the strut.

Doing this for each segment results in 248 equations (plus two boundary conditions) which can be solved yielding the temperature profile shown in Figure 3.5-2. The strut radiates effectively due to its black side, but only absorbs 0.02 of the thermal radiation hitting it. Consequently, this—coupled with the poor thermal conductivity of titanium—causes the temperature profile to drop quickly, so that within 50 cm the strut reaches an equilibrium condition where minimal heat flows along the strut and its temperature is determined by the equilibrium between the thermal power absorbed and that radiated. For the case shown this equilibrium temperature is slightly less than 300 K resulting in no heat being transferred to the vehicle.

A more rigorous analysis would include shielding by the cone, reducing the thermal load on the strut, and dropping its temperature further. Though in this region it might be prudent to cover the entire strut with a high emissivity coating in order to not reflect heat back at the vehicle. The net result of making these two changes is minimal; the conclusion being that a properly designed strut conveys little or no heat to the vehicle. Radiant heat loss by a high emissivity, high temperature object, is very effective at providing rapid cooling.

3.6 The Need for a Curved Shield

It was shown above that the Solar Probe design shown in Figure 3.4-3 can approach the Sun to about 1.4 solar radii from the Sun’s center without excessive temperatures being reached on the shield or excessive heat load on the payload. In addition, it was shown above that heat conduction along the struts to the payload are not significant. However, the design shown cannot approach the Sun to this close a distance due to the apparent size of the Sun; at this distance the Sun would fill so much of the vehicle’s field of view that sunlight would hit the payload passing around the outside edges of the shield. The situation is shown schematically in Figure 3.6-1, where, for the size specifications shown in Figure 3.5-1, the minimum approach distance to the Sun is 1.67 solar radii. At closer approach distances light from the edges of the apparent Sun can approach the vehicle at an angle steeper than the strut angle; the struts define the angle between the edge of the shield and the back corner of the payload. So at these closer distances the shield is not large enough to block the Sun and solar irradiance begins to directly hit the vehicle’s payload.

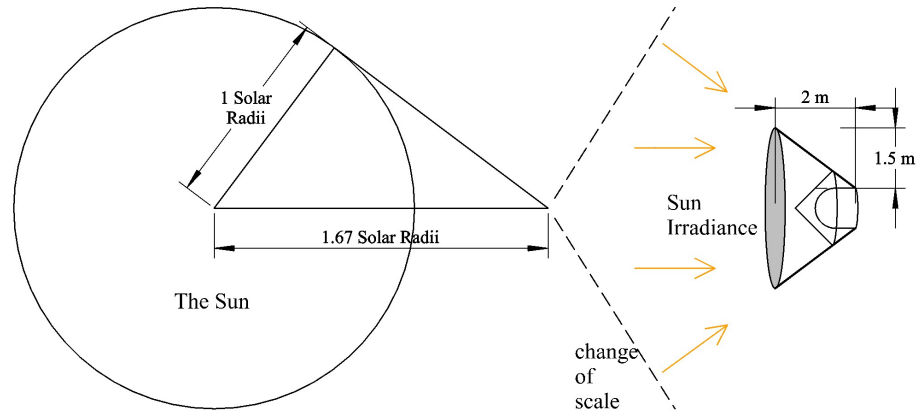


Figure 3.6-1. The slope of the struts sets the closest approach distance to the Sun at 1.67 solar radii. Approaching closer than this allows the solar irradiant power to hit the payload due to the large apparent size of the Sun.

A suggested solution to this problem is to curve the shield. Figure 3.6-2 shows an extreme case where the shield is curved sufficiently to block solar radiation coming in from nearly the full half sphere, i.e. from the sun’s apparent size as seen from its surface, or in the transition zone. The problem with this approach is that it collects solar power across the entire shield area, which is larger than the flat shield, but must emit that energy out of an opening that is similar or smaller in size. Consequently, since the analysis above showed a minimal approach distance of 1.4 solar radii with a flat shield, using a curved shield would increase this distance, assuming no significant design changes.

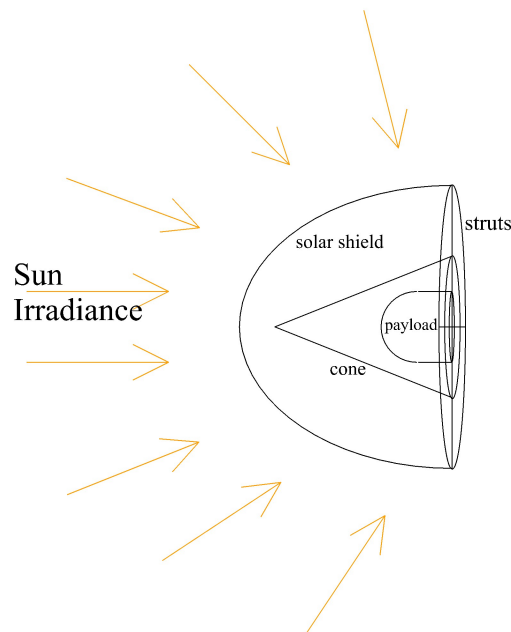


Figure 3.6-2. A strongly curved solar shield blocking the Sun’s irradiant power from a very wide angular range.

3.7 Additional Thoughts

The discussion above yields a minimum approach distance to the Sun of about 1.6 solar radii from the Sun's center. This assumes some slight curvature added to the shield in order to block the tangential rays of the Sun from hitting the payload. Yet not so much curvature that the infrared emission given off of the shield exceeds the allowable heat load on the payload.

So can we get closer than this? We may be able to find a better material or, assuming a highly elliptical orbit, show that the vehicle is not heated long enough to cause a payload thermal problem. Also, it may be possible to add more reflectors between the shield and the spacecraft.

3.7.1 Alternative Materials

Most of the discussion above assumed BaF_2 as the shield material since this is to-date the optimal material in terms of transmission band and manufacturability. However, there are other possible materials, as described in Appendix I. This appendix calculates the temperature of a flat plate coated with scattering particles of various materials with a highly emissive black coating on the back of the plate. When this appendix was written we believed that the most important parameter was whether the shield material would survive the temperatures near the surface of the Sun and we prepared the plot shown in Figure 3.7.1-1. The straight line in this plot shows whether a material will melt (below the line) or not (above the line) near the surface of the Sun. However, this is misleading, the particle nature of these materials mean that they will sinter, causing the coating to change form at temperatures well below their melting temperature. The actual limit is not known for each material since this depends on particle size (for BaF_2 we sinter at 1050 K, well below the melting point (about 1600 K)), and would not recommend long term use at temperatures above about 850 K.

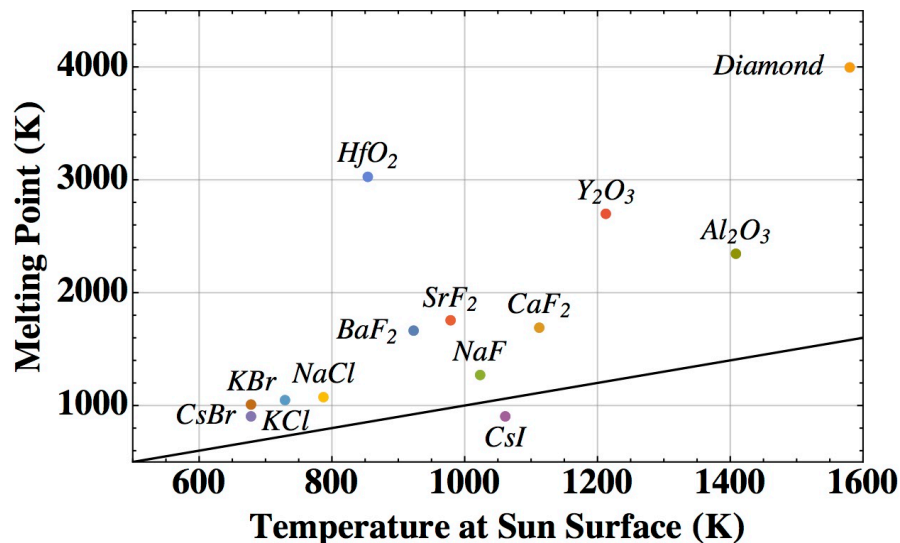


Figure 3.7.1-1. Plot comparing the performance of different scattering materials at the Sun's surface with a 1 cm thick coating. Diamond is the exception with a 100 μ m thick coating.

So one might assume, from Figure 3.7.1-1, that diamond is an ideal material because its melting point is so far above its shield temperature. However, as was shown in the discussions above, the limitation in approaching the Sun is not necessarily the survivability of the shield, but the ability to protect the payload from the infrared emission given off by the shield. Recognizing this, one might then suggest CsBr, KCl, or KBr as possible materials, since they minimize the shield temperature and hence the infrared load on the payload. Figure 3.7.1-2 shows the predicted temperatures of a plate coated with KBr as a function of distance from the Sun's center. Note that these

temperatures are lower than those seen by the BaF₂ shield and thus place less infrared burden on the payload. However, KBr melts at 1000 K and we have sintered it at 700 K. Our team recommends that KBr not exceed 650 K, which from Figure 3.7.1-2, yields a 1.5 solar radii approach distance, not too different from that of BaF₂. So there is no gain from using KBr due to its low melting point.

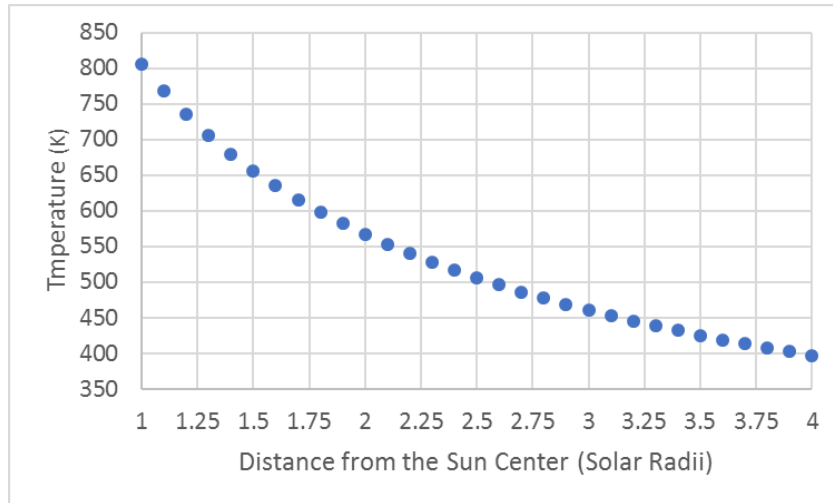


Figure 3.7.1-2. This plot shows the temperature of a flat solar shield with a 1 cm thick layer of KBr particles on the solar side and a high emissivity coating on the back side as a function of distance to the Sun.

We are currently considering Hafnium Oxide and Yttrium Oxide as possible materials. We do not have good optical data on these materials, but the literature and the material properties indicate that they might yield a significantly lighter and more survivable shield. But with this uncertainty, we currently cannot claim that any material significantly improves upon the performance of BaF₂.

3.7.2 Transient Thermal Response

If we assume a highly elliptical orbit around the Sun, say an orbit like the Parker Solar Probe where one perihelion is at 2 solar radii from the Sun’s center and aphelion is at Venus, then we may be able to get closer to the Sun by operating in a short time duration. If we assume the spacecraft weighs about 500 kg (like the Parker Solar Probe) and has an absorption area of about 1 square meter, can tolerate a 10 degree rise, and has an averaged heat capacity of 1 Joule/(gm-K) (similar to aluminum), then the spacecraft can absorb 5,000,000 Joules over a short time period, assuming it can radiate this away when it is further from the Sun.

Orbital calculations show that the spacecraft is moving at 430 km/sec at perihelion. Figure 3.7.2-1 shows a scaled drawing of the orbit of the spacecraft (eccentricity is 0.975). Note the small arc in the drawing. This arc has a radius of 4 solar radii and an arc length of 90 degrees, so its physical length is $4(\pi/2) \approx 6.3$ solar radii. One solar radius is about 700,000 km so this arc is about 4.4 million kilometers. So it takes approximately 3 hours for the spacecraft to fly through this near Sun region. Using the 5,000,000 Joule number from above, this means the spacecraft can absorb about 460 Watts of additional power during this time.

Recall that the BaF₂ coating was near its sintering temperature, so what this new insight provides is the ability to operate the shield with a material that can become hotter without damage for a short time period. Future work will

keep this in mind when considering novel materials, such as those listed in Appendix I. A transient approach such as this might allow the surface of the Sun to be touched.

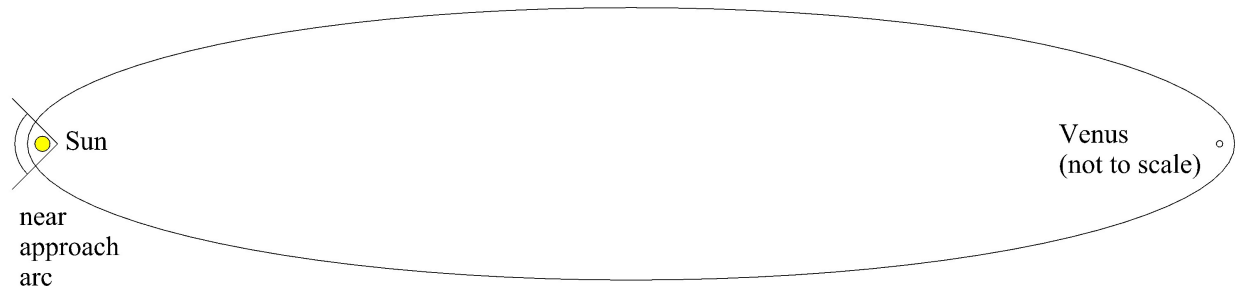


Figure 3.7.2-1. This is a plot of the orbit of the spacecraft traveling within 1 solar radii of the surface of the Sun and then passing by Venus. The Sun and orbit are to the same scale, but Venus is not to scale.

3.7.3 Additional Shields

It may be possible to add additional infrared shields, similar to the approach used on the James Webb Telescope solar shield, to reduce the heat reaching the vehicle from the outer shield. We have not explored this option due to lack of time and a sense that the gains achieved will be minimal. The heat load on the vehicle might be lowered, but at the expense of reflecting energy back towards the outer shield and increasing its temperature.

4. EXPERIMENTAL WORK

In our proposal we stated that we would work with the Johns Hopkins University Applied Physics Lab (JHU/APL) to test the response of our new shielding material when exposed to an 11x solar simulator. When our project was awarded (May 2017) we initiated a request to procure services from the JHU/APL and this request went through our procurement process quickly (June 2017). However, when it reached JHU/APL our partner did not know how to accept the funds. After more than 2 months of effort a funding route was found (August 2017), but we were told that it would require starting over and we were told that the paperwork could not start until the beginning of the next fiscal year (Oct 2017). We were also told that the paperwork, once started, would not be complete for two months (December 2017). Due to the holidays, work at JHU/APL would likely not start until January 2018 and the project final report was due in February 2018. So we decided to cancel this portion of the work. The funds set aside for the JHUAPL testing (\$40K) were reassigned to cover additional testing and modelling. The experimental work, including advances in coating fabrication and in optical testing, are described below.

4.1 High Irradiance Sample Preparation

When the project was awarded in May we contacted JHU/APL and were told that a large area sample was required for testing in their 11x solar simulator. They needed a sample that was three inches in diameter, but this

was substantially larger than any samples we had previously created. So we machined molds, modified our processes, and worked our way up to the sample shown in Figure 4.1-1, which is 6.3 mm thick and 86 mm in diameter. A substantial silver layer was deposited on the back. The aluminum mount was primed with SS 4004P and the same RTV used to attach Shuttle tiles to the Orbiter (RTV560) was used to glue the coating to the aluminum.

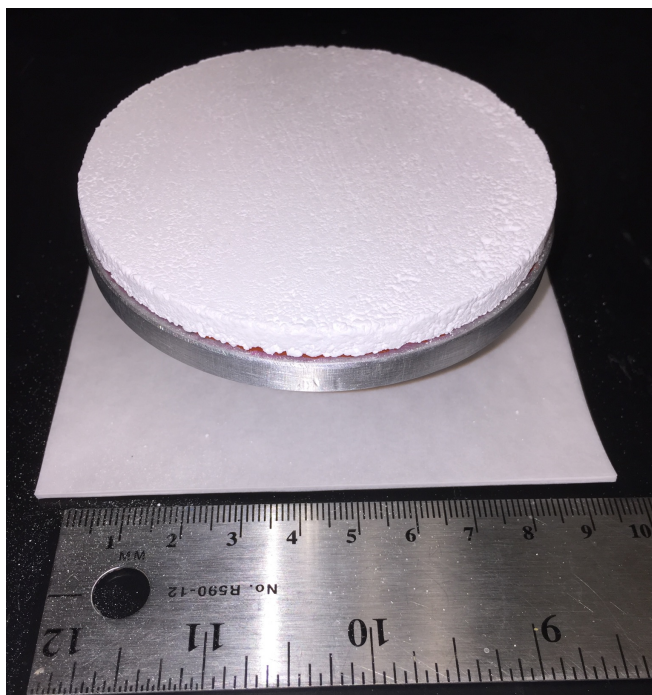


Figure 4.1-1. A piece of our high reflectivity coating mounted to an aluminum base.

It should be mentioned that these rigid coatings are fabricated by mixing water with BaF_2 powder to form a paste. The paste is then pressed into a ceramic mold and transferred into an oven. The oven is slowly raised in temperature to remove the water and allow the particles to sinter, forming a rigid entity. The sintering process causes the particles to move together, i.e. the final rigid sample is smaller by about 15% than the mold. This shrinkage is a source of concern for large samples because at some size we expect the entity to pull apart during the sintering process and yield two or more rigid pieces. Fortunately, this did not occur for the 3-inch sample shown in the Figure. Further details on the fabrication process are described in the upcoming final report for our Phase 2 NIAC on cryogenic selective surfaces.

4.2 Improved Coating Material

During the summer of 2017, when we were expecting to fabricate multiple large samples, we placed an order for BaF_2 powder. Up to this point all of our BaF_2 powder had been obtained from Sigma-Aldrich (precipitated, 99.999% pure, item number 652458, 100 gm is about \$200). However, Sigma-Aldrich was unable to deliver the material due to a backorder issue and we had to search for an alternative source. This led to some concern, not only about material availability, but a re-evaluation of particle size. We located some new sources that could supply very pure BaF_2 powder, but the powder grains were large and even with very long grinding times the very small size particles needed for our application were not being achieved. Ideally, from Mie scattering theory, in order to scatter light of a given wavelength the particle circumference should match that wavelength. So if the Sun's spectrum peaks

around 500 nm an ideal particle would have a diameter of about 160 nm. The Sigma-Aldrich powder size was smaller than that supplied by the other vendors, but not this small.

The KSC chemists, under Dr. Tracy Gibson, found a paper describing a process for precipitating BaF_2 particles by mixing Barium Nitrate and Ammonium Fluoride [29]. By following a modified form of this procedure, they were able to synthesize BaF_2 crystals to a smaller size than that supplied by any of the vendors. Figure 4.2-1 shows Scanning Electron Microscope (SEM) images of the Sigma-Aldrich powder (left) and the KSC precipitated powder (right). Many of the Sigma-Aldrich particles are nearly 1 micron in size. The KSC particles are more uniform in size and are mostly in the 200-600 nm diameter range.

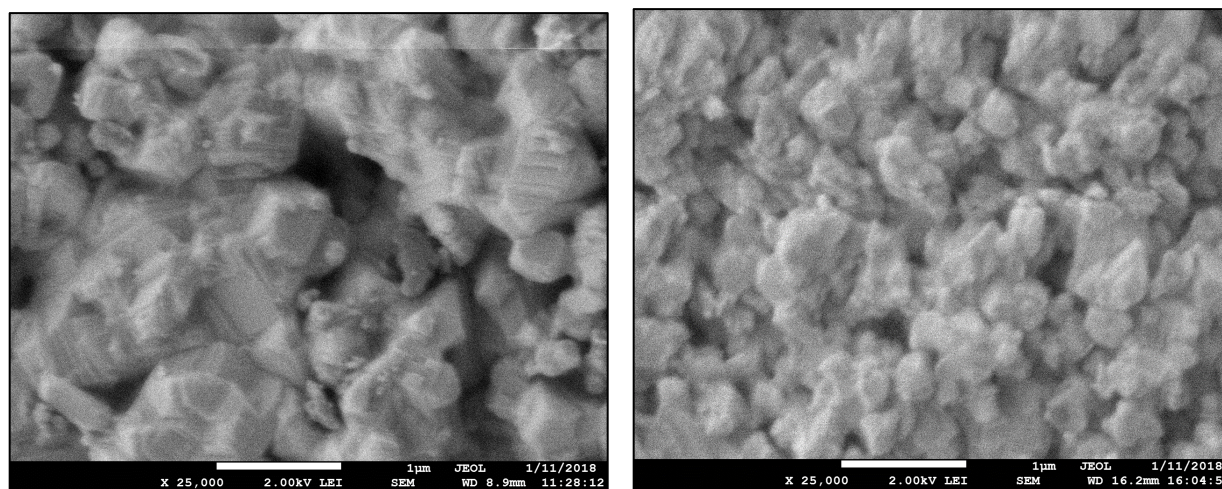


Figure 4.2-1. Scanning Electron Microscope images of Sigma-Aldrich BaF_2 powder (left) and powder prepared at KSC (right).

These new powders were used to create rigid samples. Figure 4.2-2 shows SEM images of the surface of two rigid samples, one fabricated from Sigma-Aldrich powder and one from the smaller KSC powder. In both cases the rigid sample particles appear larger on average than for the powders, which is likely a result of the sintering process fusing the smaller particles together. The particles in the rigid sample made from the KSC powder are smaller, but are still too large, so we began to vary the fabrication process to try and reduce the particle size further.

We started by chilling the compounds used to make the powder thinking this might slow down the reaction and make the particles smaller. That did not happen. Instead they got larger as seen in the left image of Figure 4.2-3. So then we tried diluting the chemicals used in the process and that also did not help. As seen in the image on the right side of Figure 4.2-3, this yielded large particles with very clean faces, indicative of the cubic structure formed by this compound. We also tried varying the addition rate and the temperature of the chemicals and this did help. Figure 4.2-4 shows particles resulting from warm chemicals and an SEM of a sintered block composed of these particles. They are starting to reach the desired size range of 150-200 nm diameters. Finally Figure 4.2-5 shows the particles generated by heating the chemical to 45° C. Work is currently proceeding on determining what the correct process should be to generate particles in the desired size range.

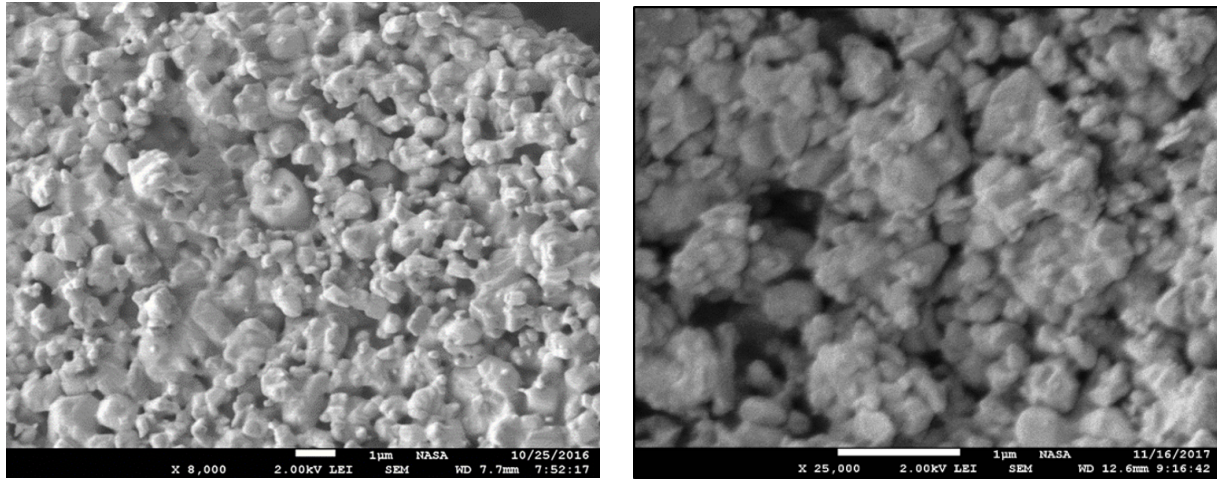


Figure 4.2-2. Scanning Electron Microscope images of two rigid coating samples, the left fabricated from Sigma-Aldrich BaF_2 powder and the right from powder prepared at KSC.

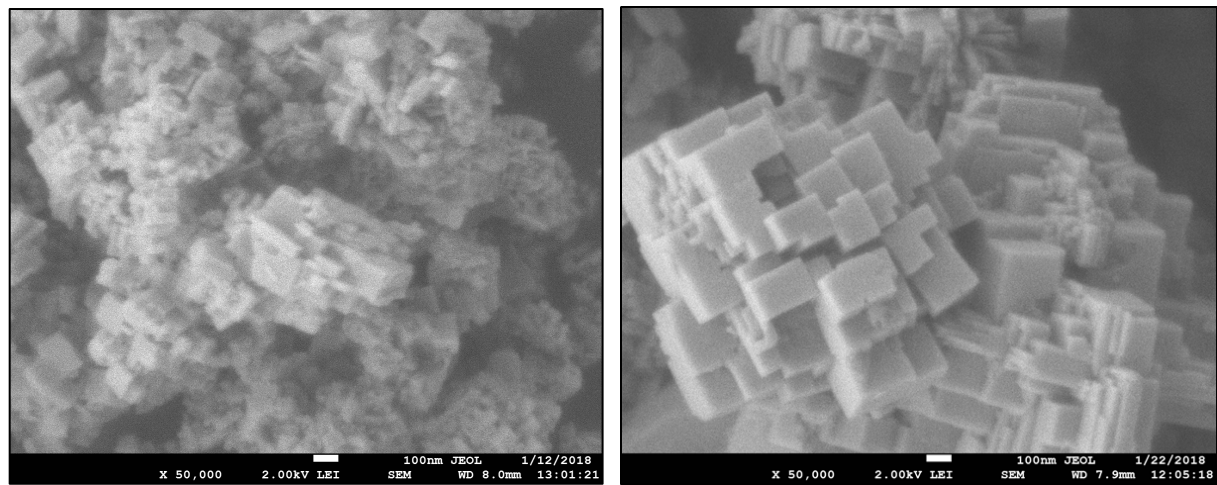


Figure 4.2-3. Barium Fluoride (BaF_2) nanocrystals produced by reducing the temperature of the process (left) and by diluting the chemicals in the process (right). The particles are still too large.

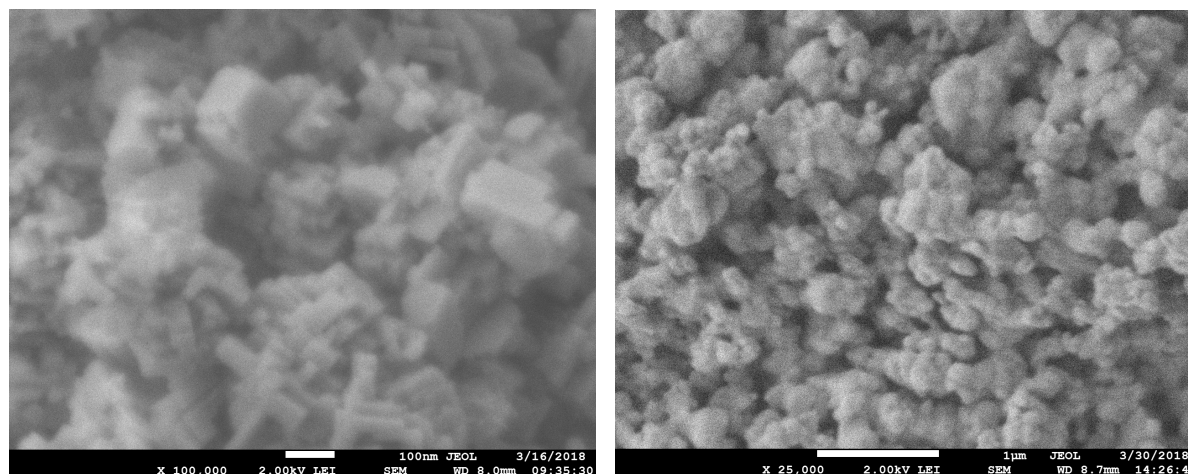


Figure 4.2-4. Barium Fluoride (BaF_2) nanocrystals produced by increasing the temperature of the process (left). The image on the right is a sintered solid form from the particles shown on the left.

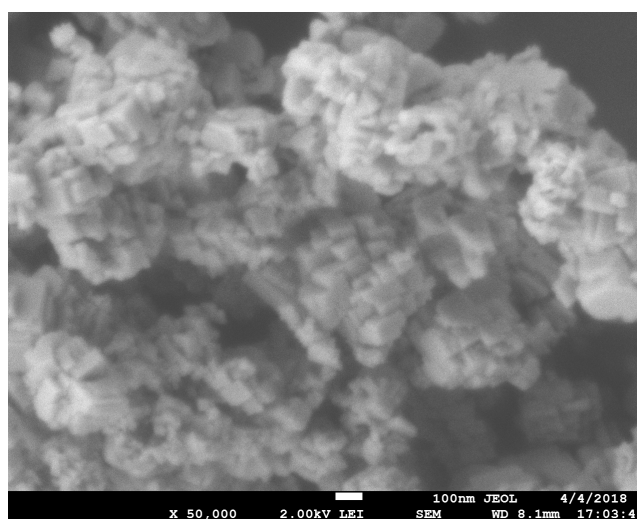


Figure 4.2-5. Particles made with 45°C chemicals.

4.3 Reflectance Measurements

One of the reasons for moving away from the Sigma-Aldrich powder is that the large particles cause enhanced reflectivity in the near infrared, but do not scatter light as well in the ultraviolet and visible regions of the spectrum. The Sun's peak irradiance is in the visible so ideally we would like particles about 150 to 200 nm in diameter to best scatter this wavelength range and the Sigma-Aldrich particles are larger than this. The previous section showed sample SEM photos of the powders and rigid samples, but these only represent a tiny portion of the material's surface. A possibly better indication of performance is to measure the reflectance of the sintered samples. Figure 4.3-1 shows the measured reflectance spectra of two rigid BaF_2 samples made with the Sigma-Aldrich powder compared to Spectralon (the blue line), a NIST standard [33]. Both samples show poorer scattering than Spectralon in the ultraviolet and visible (out to about 700 nm) and have similar scattering (reflectivity) in the near-infrared. It should be pointed out that the slight dip around 1400 nm appears to be due to a spectrometer issue

associated with misplacing the scatterer (this dip can be generated by slightly moving the Spectralon reference) and the variation between the two samples may also be due to small position variations.

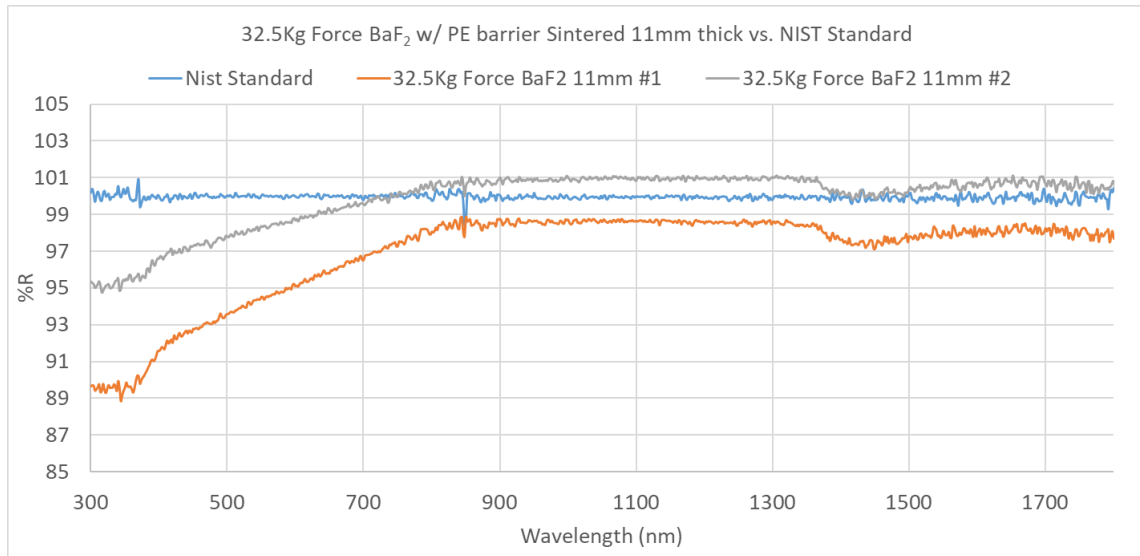


Figure 4.3-1. These are plots of the reflectance spectra of rigid BaF₂ samples made with the Sigma-Aldrich large particles.

Figure 4.3-2 shows the reflectance spectra of three rigid samples made with synthesized BaF₂, all compared to Spectralon. These rigid samples were composed of powder synthesized in our lab using normal concentration and room temp conditions (the 12127 sample), using dilute materials (the Dil sample), and using cold materials (the cold sample). These synthesized generated particles have more small particles (as verified in the SEM photos) and cause higher reflectivity in the ultraviolet than that of the NIST standard. It is not clear if the variations seen in the visible here are real or are due to positioning variations inside of the spectrometer, but the overall increase in short wave reflectivity as compared to the Sigma-Aldrich powder based samples is clear.

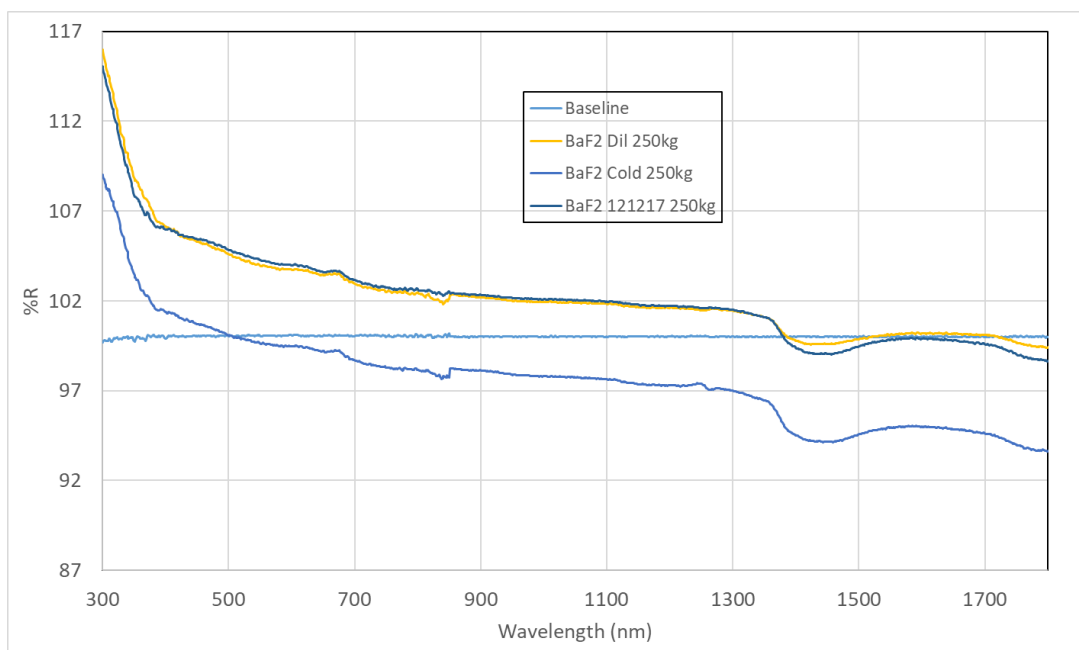


Figure 4.3-2. These are plots of the reflectance spectra of rigid BaF₂ samples made with synthesized BaF₂ powder.

4.4 High Irradiance Testing and Water Issues

When the attempt to contract with the Johns Hopkins University Applied Physics Laboratory failed, we decided to perform high irradiance testing at KSC. We obtained a relatively inexpensive Xenon light source, see Figure 4.4-1, and verified with an Ocean Optics spectrometer that the output contained significant UV radiation and peaked near 0.5 microns, so this can be considered a rough simulation of the Sun's irradiance. The output from this instrument was focused onto a temperature monitored sample of sintered BaF₂ and we saw that the sample heated more quickly than expected. The results showed that it was gaining energy at roughly ten times the predicted rate.



Figure 4.4-1. A Xenon light source that generates an approximate solar spectrum.

The first possible source of this extra heating is infrared emission. The light source generates a large amount of infrared radiation, far more than the Sun in proportion to its visible emission. So various infrared heat blocks were installed and some reduction in the heating was seen, but not enough to explain the discrepancy. It was then observed that the scattered light (most of the light hitting the sample is scattered) was warming the lens holder and its IR emission was causing more heat load, but this still didn't resolve the issue. We then started considering water.

Water can bond to the surfaces of BaF₂ crystals [31, 32] forming very thin layers, up to three molecules thick (about 1 nm). This isn't much water, but the structure has a very large surface area and the light interacts with that surface thousands of times on average, yielding a net water interaction length that could be several microns in thickness. We modeled the absorption of solar energy by water by calculating the absorption of small wavelength intervals of the sun's irradiance spectrum using known water absorption data and then integrating the result. This result is shown in Figure 4.4-2.

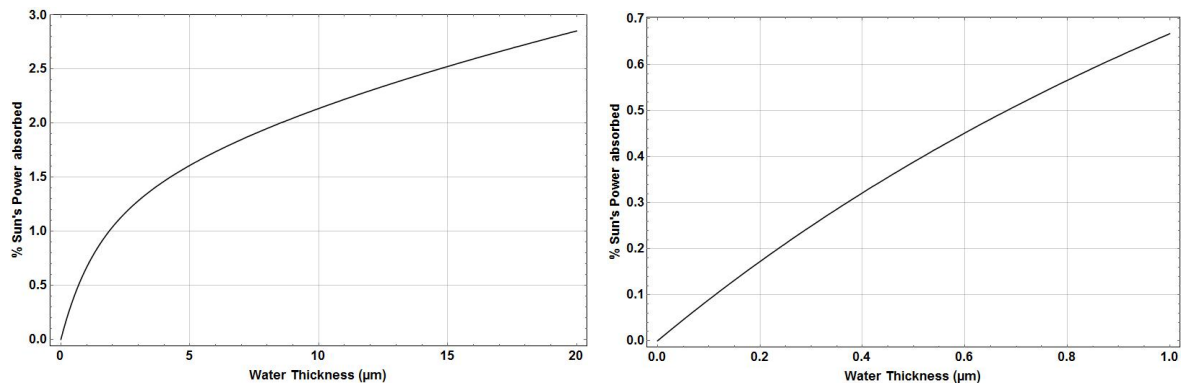


Figure 4.4-2. The amount of the Sun's power absorbed by a thin layer of water. The plot to the right is an enlargement of the plot on the left.

From this Figure it is seen that about 2-8 microns of water will absorb between 1% and 2% of the Sun's irradiance power, which is far too much for our application and necessitates removing the water. We desire to have less than 0.1% absorption indicating a maximum thickness of water of about 0.1 micron, a 99% reduction. We located a paper on the adsorption of water vapor by Barium Fluoride [31] which indicated that complete removal of water from a pressed disk of powdered BaF₂ could be achieved by heating in a vacuum to 673 K (400° C). This paper then stated that after this, if the BaF₂ was exposed to humid air, that the adsorbed water could be removed by evacuation at room temperature—heating would not be required. Since all of our uses assume operation in the vacuum of space this would be a desired result, we would desire that a properly prepared sample of BaF₂ would lose its water when exposed to vacuum.

The detection and removal of water from sintered BaF₂ was studied (see Appendix II) and sadly, the conclusions were inconclusive. It is not known if the BaF₂ coating will completely dry when held under vacuum. Under our Phase 2 NIAC we exposed BaF₂ to ultraviolet light when under vacuum and saw minimal absorption, however, the wavelength of light being used, 375 nm, is poorly absorbed by water. So this test does not clarify the situation. Under our Phase 2 NIAC we will be performing this test again with a solar simulated light source and will hopefully gain more insight into this issue.

If we find that BaF₂ will not dry in vacuum, this is not a serious issue for solar surfing because the shield will then heat in the presence of the Sun and the water will be driven off (the testing described in Appendix II has shown that heating the BaF₂ to 260° C will drive off the water). In addition, we are currently considering materials such as HfO₂ and Y₂O₃ that are hydrophobic and should retain very little water under vacuum.

4.5 MISSE10

After communicating with the Parker Solar Probe Heat Shield Design Team, we requested a NASA contact at Goddard that could work with us. Our goal was to begin the process of transitioning the solar surfing concept to Goddard for consideration in a future solar probe. Mark Hasegawa agreed to be our Goddard contact and after some exchange of information Dr. Hasegawa told us that a plate of thermal coatings was being sent to the ISS as part of MISSE10, the Materials International Space Station Experiment. He offered a slot on that plate to us and asked that we generate four samples of our BaF₂ coating material, one would fly, one was a control, and two were backups.

The samples were fabricated using a ceramic mold and synthesized barium fluoride nanocrystals and the sintering process. They were shaped and RTV 560 was applied to the back of each sample. Each sample was then placed into an aluminum holder that had been coated with primer SS 4004P, see Figure 4.5-1. A weight was applied to the top of each sample to ensure good contact between the sample and the holder during the curing process (about 24 hours duration). An example of a final mounted sample is shown in Figure 4.5-2, along with a photo of the four packaged and delivered samples.



Figure 4.5-1. Five aluminum sample holders coated with primer.

Typical properties for these MISEE10 coating test articles are:

- Sample Properties
 - Weight: 1.4134 grams
 - Diameter: 15.75 mm
 - Thickness: 3.02 mm
 - Void Volume: 50.91%
- Mounted Sample Properties
 - Mass of Holder + Primer: 1.2299 grams
 - Mass of Mounted Sample: 2.6658 grams
 - Mass of Applied RTV: 0.0225 grams
 - Weight Applied for Curing RTV: 45.9 grams

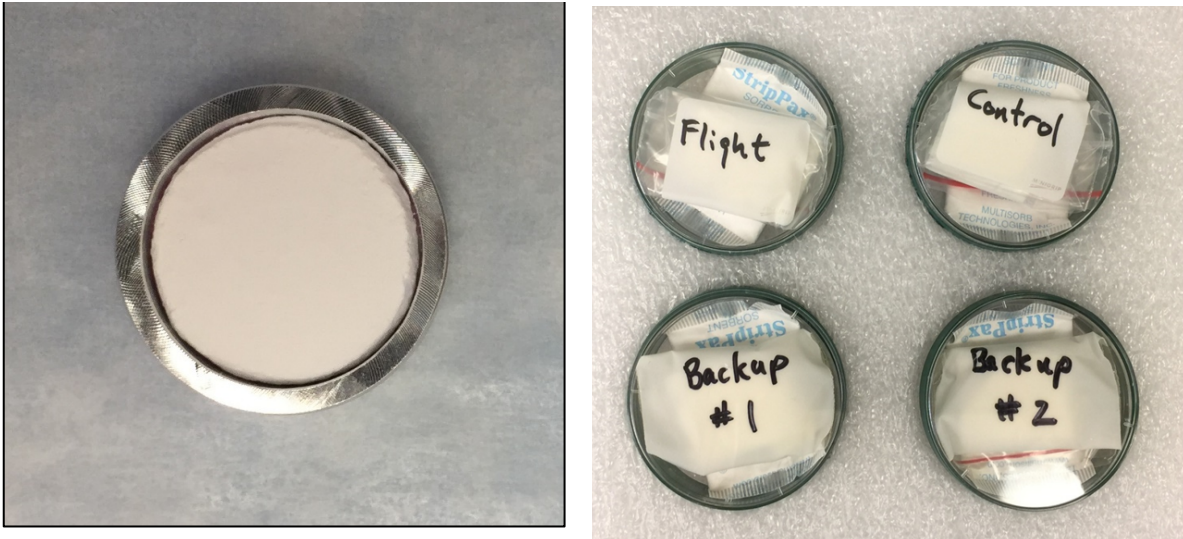


Figure 4.5-2. Photos of a complete mounted sample and the four packaged samples that were delivered to Goddard for MISEE10.

5. FUTURE WORK AND CONCLUSIONS

5.1 New Mission Possibilities

After presentation of the solar surfing concept at the 2017 NIAC Symposium, two new missions that are based on near Sun approach were brought to our attention by JPL representatives. The first was from the physics community where it was pointed out that a refined test of General Relativity could be performed if a future spacecraft could be located near the Sun, deep in its gravitational well. The force of gravity near the Sun is 28 times that of being near the earth so a corresponding improvement in the testing of General Relativity could be performed.

The second is based on an observation from JPL that the only way for a significantly massed vehicle to reach interstellar space in a reasonable time period (under 40 years) is to slingshot around the Sun. However, analysis shows that to do this effectively the vehicle must pass within 3 solar radii of the Sun [34° and that cannot be achieved with current technology. The concepts developed in this Phase I NIAC are required and the JPL team has been in contact with the authors, gaining insight into our progress and current status. It is also interesting to note that the JPL team is considering using the Sun's heat to heat hydrogen to 3400 K and use it as a propellant while near the Sun, (Oberth effect) to achieve additional delta-v.

5.2 Future Work

There is substantial work ahead in three areas. The coatings need to go through further development including optimizing thickness versus optical performance, optimizing strength, sealing the surface, resolving the water issue (this might lead to the use of new coating materials such as Hafnium Oxide or Yttrium Oxide), and testing them under high illumination. Then, various space-based tests are needed to ensure the coating will not change optical properties while in space; e.g. radiation exposure, solar wind exposure, and that the material will survive launch (vibration and acoustic loading testing along with non-particle producing testing). Finally, mission analysis is needed to further show how this new coating would be used on a future solar probe, general relativity experiment, or solar sling shot mission.

5.3 Conclusions

This study has demonstrated that a powder based coating, potentially composed of BaF₂ could be used on a future solar probe to approach the Sun to less than 1 solar radius of the Sun's surface. This would be a significant advance over the current state-of-the-art as demonstrated by the Parker Solar Probe which is predicted to reach about 8 solar radii from the Sun's surface. However, heating of the shield, the need to curve the shield, and the heat load on the vehicle all play roles in preventing much closer approach. So we did not generate a design that would allow the transition region to be reached—but this might still be possible. There is still a possibility that by using a higher melting point material (such as Hafnium Oxide or Yttrium Oxide) it might allow the heat shield to survive a very close approach to the Sun and then by using a transient analysis it might be possible to show that a brief dip into the transition region, traveling at an enormous speed, might be possible.

6. REFERENCES

1. Wikipedia contributors, "Solar wind," *Wikipedia, The Free Encyclopedia*, https://en.wikipedia.org/w/index.php?title=Solar_wind&oldid=800200791 (accessed October 6, 2017)
2. Wikipedia contributors, "Corona," *Wikipedia, The Free Encyclopedia*, <https://en.wikipedia.org/w/index.php?title=Corona&oldid=803253755> (accessed October 6, 2017).
3. Wikipedia contributors, "Solar transition region," *Wikipedia, The Free Encyclopedia*, https://en.wikipedia.org/w/index.php?title=Solar_transition_region&oldid=686084548 (accessed October 6, 2017).
4. Wikipedia contributors, "Helios (spacecraft)," *Wikipedia, The Free Encyclopedia*, [https://en.wikipedia.org/w/index.php?title=Helios_\(spacecraft\)&oldid=803275850](https://en.wikipedia.org/w/index.php?title=Helios_(spacecraft)&oldid=803275850) (accessed October 6, 2017).
5. Wikipedia contributors, "TRACE," *Wikipedia, The Free Encyclopedia*, <https://en.wikipedia.org/w/index.php?title=TRACE&oldid=792139384> (accessed October 6, 2017).
6. Wikipedia contributors, "Solar Orbiter," *Wikipedia, The Free Encyclopedia*, https://en.wikipedia.org/w/index.php?title=Solar_Orbiter&oldid=804059451 (accessed October 6, 2017).
7. Wikipedia contributors, "Parker Solar Probe," *Wikipedia, The Free Encyclopedia*, https://en.wikipedia.org/w/index.php?title=Parker_Solar_Probe&oldid=804035653 (accessed October 6, 2017).
8. "Solar Probe, Thermal protection System, Risk Mitigation Study, FY 2006 Final Report", The John Hopkins University Applied Physics Laboratory, Laurel, Maryland, contract NAS5-01072.
9. Congdon, Elizabeth A., Douglas S. Mehoke, Mark Buchta, Dennis Nagle, Dajie Zhang, and James B. Spicer. "Development of a High-Temperature Optical Coating for Thermal Management on Solar Probe Plus." In *10th AIAA/ASME Joint Thermophysics and Heat Transfer Conference*, vol. 28. 2010.
10. Dupont document, DuPont™ Ti-Pure® titanium dioxide, Titanium Dioxide for Coatings, https://www.chemours.com/Titanium_Technologies/en_US/tech_info/literature/Coatings/CO_B_H_65969_Coatings_Brochure.pdf.

11. J.H. Henninger, "Solar Absorptance and Thermal Emittance of Some Common Spacecraft Thermal-Control Coatings," NASA Reference Publication 1121 (Apr 1984).
12. "Spacecraft Thermal Control and Conductive Paints/Coatings and Services Catalog," AZ Technology, Huntsville, AL (Jan 2008).
13. Grum, F., and G. W. Luckey. "Optical sphere paint and a working standard of reflectance." *Applied Optics* 7, no. 11 (1968): 2289-2294.
14. Kubelka, Paul, and Franz Munk. "An article on optics of paint layers." *Z. Tech. Phys* 12, no. 593-601 (1931).
15. Youngquist, Robert C., and Mark A. Nurge. "Achieving cryogenic temperatures in deep space using a coating." *Optics letters* 41, no. 6 (2016): 1086-1089.
16. Youngquist, Robert C., and Mark A. Nurge, "Cryogenic Selective Surfaces", Final Report on a Phase I NIAC Study, Feb. 2016.
https://www.nasa.gov/sites/default/files/atoms/files/cryogenic_selective_surfaces_final_report_niac_phase_i.pdf
17. Wikipedia contributors, "Kirchhoff's law of thermal radiation," *Wikipedia, The Free Encyclopedia*, https://en.wikipedia.org/w/index.php?title=Kirchhoff%27s_law_of_thermal_radiation&oldid=802098324 (accessed October 16, 2017).
18. R.R. Hibbard, "Equilibrium Temperatures of Ideal Spectrally Selective Surfaces," *Solar Energy* 5(4):129-132 (Oct-Dec 1961).
19. Qioptiq Inc. information on optical solar reflectors. <http://www.qioptiq.com/space.html>
20. *Handbook of Optical Constants*, ed. Edward D. Palik, 5 vols, San Diego, CA: Academic Press (1997).
21. Li, H. H. "Refractive index of alkali halides and its wavelength and temperature derivatives." *Journal of physical and chemical reference data* 5, no. 2 (1976): 329-528.
22. Martienssen, Werner. "Über die excitonenbanden der alkalihalogenidkristalle." *Journal of Physics and Chemistry of Solids* 2, no. 4 (1957): 257-267.
23. Stolen, Rogers, and Klaus Dransfeld. "Far-infrared lattice absorption in alkali halide crystals." *Physical Review* 139, no. 4A (1965): A1295.
24. Meijer, A. S., J. J. H. Pijpers, H. K. Nienhuys, M. Bonn, and W. J. van der Zande. "A THz spectrometer based on a CsI prism." *Journal of Optics A: Pure and Applied Optics* 10, no. 9 (2008): 095303.
25. Thomas, Michael E. "A computer code for modeling optical properties of window materials." In *Window and Dome Technologies and Materials*, vol. 1112, pp. 260-268. International Society for Optics and Photonics, 1989.
26. Thomas, Michael E., and Richard I. Joseph. "A comprehensive model for the intrinsic transmission properties of optical windows." In *Infrared Optical Materials IV*, vol. 929, pp. 87-94. International Society for Optics and Photonics, 1988.
27. Hoffmann, Christian. "Optical constants of infrared active phonons as a function of frequency and temperature." PhD diss., Johns Hopkins University, 1989.
28. de Silans, Thierry Passerat, Isabelle Maurin, Pedro Chaves de Souza Segundo, Solomon Saltiel, Marie-Pascale Gorza, Martial Ducloy, Daniel Bloch, Domingos de Sousa Meneses, and Patrick Echegut. "Temperature dependence of the dielectric permittivity of CaF₂, BaF₂ and Al₂O₃: application to the prediction of a temperature-dependent van der Waals surface interaction exerted onto a neighbouring Cs (8P_{3/2}) atom." *Journal of Physics: Condensed Matter* 21, no. 25 (2009): 255902.
29. Wu, Daxiong, Xijun Wu, Yanfei Lv, and Hui Wang. "Influence of solubility on the particle size of fluorides crystalline precipitated from aqueous solutions." *Materials Letters* 62, no. 17 (2008): 3003-3006.
30. Veiga, C., J. P. Davim, and A. J. R. Loureiro. "Properties and applications of titanium alloys: a brief review." *Rev. Adv. Mater. Sci* 32, no. 2 (2012): 133-148.
31. Ewing, George E. "Ambient thin film water on insulator surfaces." *Chemical reviews* 106, no. 4 (2006): 1511-1526.
32. Barraclough, Peter B., and Peter G. Hall. "Adsorption of water vapour by calcium fluoride, barium fluoride and lead fluoride." *Journal of the Chemical Society, Faraday Transactions 1: Physical Chemistry in Condensed Phases* 71 (1975): 2266-2276.
33. Georgiev, Georgi T., and James J. Butler. "Long-term calibration monitoring of Spectralon diffusers BRDF in the air-ultraviolet." *Applied Optics* 46, no. 32 (2007): 7892-7899.
34. Alkalai, Leon, et. al. "A vision for planetary and exoplanets science: Exploration of the interstellar medium—the space between the stars," 68th International Astronautical Congress, Adelaide, Australia, 2017.

7. APPENDIX I- MATERIALS COMPARISON FOR SOLAR SURFING

To keep from heating our solar observing spacecraft, we want to scatter as much of the Sun’s energy as possible. This requires a material that is transparent (with no absorption) from the ultraviolet through portions of the infrared spectrum. To find the best materials, we need to consider the Sun’s spectral irradiance and choose materials that are transparent to as much of this spectrum as possible. The 2000 ASTM Standard Extraterrestrial Spectrum Reference E-490-00 is presented below in Figure I-1. This model provides irradiance data from 0.1195 microns in the deep ultraviolet to 1000 microns in the far infrared. Other than a small spike in the deep UV and some minor structural variations, the Sun’s irradiance is similar to that of a 5778 K blackbody. The total area under this curve is 1366 W/m². Analysis shows that a material with essentially no absorption between 0.2-10 μm has the potential to back-scatter more than 99.9% of the Sun’s power.

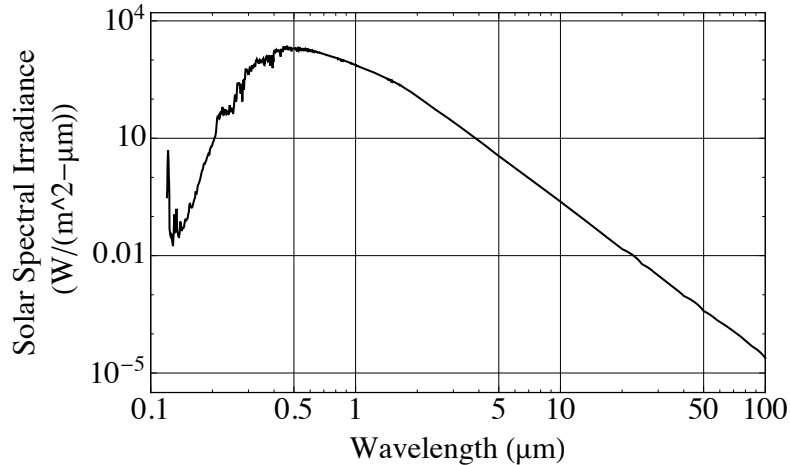


Figure I-1. This is a standard spectrum for the Sun above the atmosphere from 0.1195 microns to 70 microns.

We have elected to cover the Sun facing side of a solar shield with a particle based scattering layer over a metallic reflector (typically silver) and the side facing away from the Sun with a broadband radiator (e.g., black paint) to allow cooling of the shield. The material discussions below will use our particle based scattering model to predict the temperature that such a shield would have if located just off of the surface of the Sun. Figure I-1 above is for the Sun at 1 AU or 215 solar radii from the surface of the Sun, so the power density at the surface of the Sun will be about 215² greater than shown in the Figure.

Korth Kristalle GMBH has a webpage that allows a quick comparison of the transmission bands for 38 crystalline materials (<http://www.korth.de/index.php/material-161.html>). Crystran also has a useful site that provides transmission bands for UV and IR materials (<https://www.crystran.co.uk/optical-materials>). Transmitting over the entire band doesn’t preclude some absorption. So, we will check the absorption with available complex index of refraction data, when available. The melting points, refractive indices, and water solubility were obtained from the corresponding Wikipedia pages for the materials. The temperatures at the Sun’s surface were computed using our model for a 1 m² flat silver plate coated on one side with the scattering material and the other with a broadband emitter with an assumed emissivity of 0.9. Due to its higher steady state temperature, the CVD diamond and the oxides needed to be modeled on a tantalum reflector as silver melts at 1234 K. The complex refractive index data came from primarily two sources: The multivolume set by Edward Palik, “Handbook of Optical Constants of Solids,” and the online refractive index database at <https://refractiveindex.info>.

Barium Fluoride (BaF₂)

Barium Fluoride has a good transmission band, a higher melting point compared to others in the table, and a low solubility in water. These traits combine to make it a good all-around choice for use as a solar shield near the Sun. It occurs naturally in a mine in Nevada and is known by the name frankdicksonite, but is primarily produced synthetically. A large set of optical data is available to model its performance in our application. It is harmful if

inhaled and toxic if swallowed. The cost for 99.99% purity at one site is \$108 for 20 g. The figure below shows the approximate solar spectral irradiance at 1 AU and the absorption spectra for a 100 μm thick window made from Barium Fluoride. The steady state temperature using our model at the Sun's surface is 935 K for a flat plate design with 1 cm of BaF_2 on one side and a high emissivity coating on the other side. Adding thickness to the BaF_2 shield doesn't reduce the steady state temperature much (7cm, 924 K).

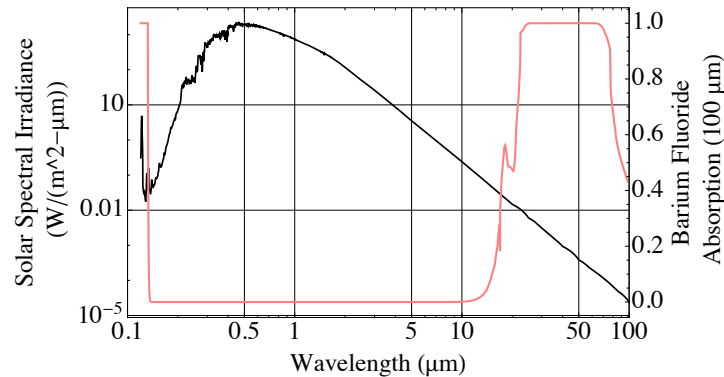


Figure I-2. The absorption curve for a 100-micron thick window of BaF_2 plotted against the Sun's spectral irradiance.

Calcium Fluoride (CaF_2)

Calcium Fluoride has a transmission band that reaches further into the UV than BaF_2 , but not as far into the IR, having a cutoff at just beyond 10 μm . Its melting point is high and is amongst the least soluble in water of the halides that were considered. Unlike BaF_2 , it has no identified hazards. It has widespread use in optical components such as windows and lenses. A large set of optical data is available to model its performance in our application. The cost for 99.99% purity at one site is \$320 for 25 g. The steady state temperature using our model at the Sun's surface is 1144 K for a flat plate design with 1 cm of CaF_2 on one side and a high emissivity coating on the other side. Increasing the CaF_2 thickness only results in a small temperature reduction (7 cm, 1113K).

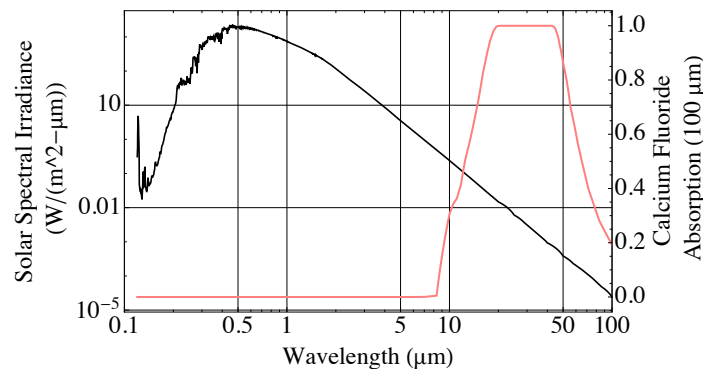


Figure I-3. The absorption curve for a 100-micron thick window of CaF_2 plotted against the Sun's spectral irradiance.

Sodium Fluoride (NaF)

The transmission band is one of the best amongst the fluorides, but has higher water solubility than many of the other fluorides. It is toxic if inhaled or swallowed, but is used as a medicine to prevent tooth decay. Some quantity is often used in toothpaste. The cost for 99.99% purity at one site is \$165 for 50 g. It has the lowest index of refraction in the table meaning it won't scatter as effectively as the other materials. The steady state temperature using our model at the Sun's surface is 1023 K for a flat plate design with 1 cm of NaF on one side and a high emissivity coating on the other side. Increasing the thickness of the NaF shield material increases the steady state temperature (7 cm, 1048 K).

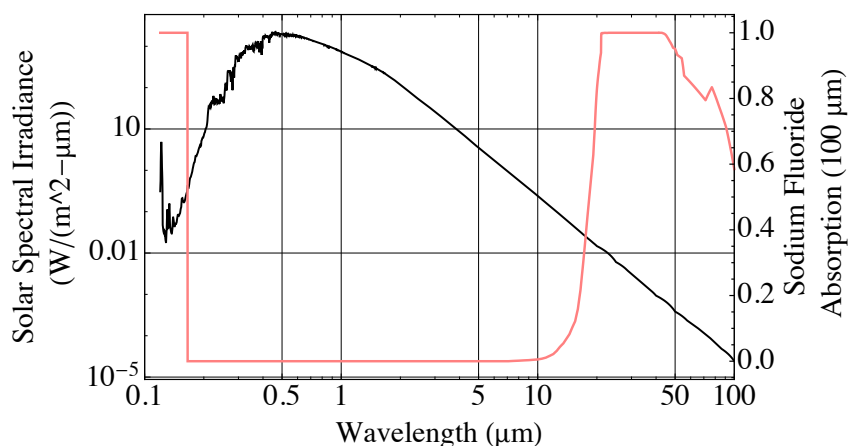


Figure I-4. The absorption curve for a 100-micron thick window of NaF plotted against the Sun's spectral irradiance.

Strontium Fluoride (SrF₂)

Strontium Fluoride has the largest transmission band of the fluorides in our table. It is also one of the least soluble halide materials and has a fairly high melting point of 1750 K while the steady state temperature using our model at the Sun's surface is 983 K for a flat plate design with 1 cm of SrF₂ on one side and a high emissivity coating on the other side. Increasing the thickness of SrF₂ to 7 cm results in a very small temperature reduction (979 K). This material is similar in performance to Barium Fluoride, but its higher melting point may make it more attractive, especially if the sintering temperature is also higher. It is an eye and skin irritant and can be harmful when swallowed or inhaled.

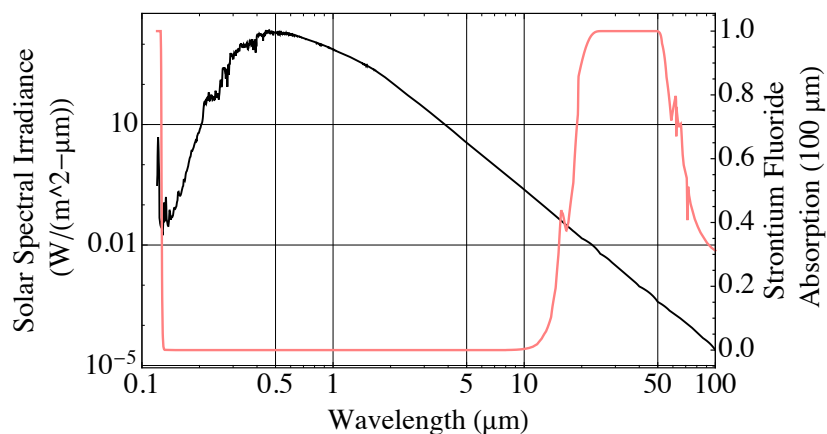


Figure I-5. The absorption curve for a 100-micron thick window of SrF₂ plotted against the Sun's spectral irradiance.

Cadmium Fluoride (CdF₂)

CdF₂ has a broad transmission band but has the highest water solubility of the fluorides considered, but it is still low compared to many of the other halides. It is toxic and can cause irritation to lungs, skin, and eyes. The cost for 99.98+% purity at one site is \$180 for 50 g. We were unable to locate a good source for the broadband complex refractive index properties needed to model it.

Lanthanum (tri)Fluoride (LaF₃)

The IR performance is about the same as CaF₂, but its UV transmittance is poorer. Attractive features are that it is insoluble in water and has a high index of refraction (better for scattering) and a high melting point. It looks like it is less common than some of the other materials. The only health warning is to avoid inhalation of the dust. The

cost for 99.99% purity at one site is \$496 for 25 g. Unfortunately, we were unable to locate a good source for the broadband complex refractive index properties needed to model it.

Cesium Bromide (CsBr)

Cesium Bromide has one of the widest transmission bands, but does absorb a bit more of the Sun's UV than the other materials. The steady state temperature using our model at the Sun's surface is 792 K for a flat plate design with 1 cm of CsBr on one side and a high emissivity coating on the other side. This melting point is also amongst lowest at 909 K, leaving little margin before the material degrades. Lower temperatures can be reached by increasing the thickness, 7 cm results in steady state temperature of 679 K, the lowest of all of our candidate materials. It has high water solubility and is toxic if ingested or inhaled and is an irritant for eyes and skin.

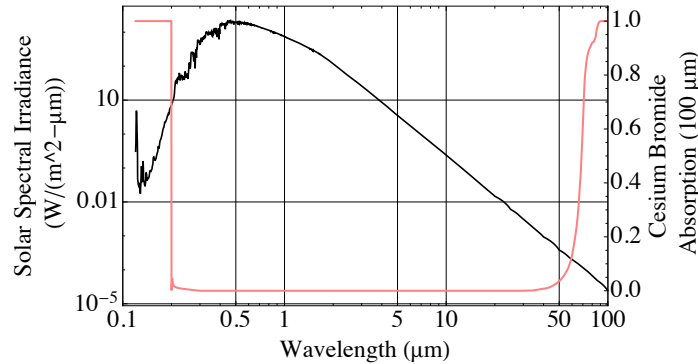


Figure I-6. The absorption curve for a 100-micron thick window of CsBr plotted against the Sun's spectral irradiance.

Sodium Bromide (NaBr)

The transmission band is much broader than for the fluorides, going out to 24 μm in the IR. It also has a higher index of refraction than most of the other halides, but has high water solubility. NaBr has a low ingestion toxicity for a single dose, but has negative cumulative effects. The cost for 99.99% purity at one site is \$490 for 100 g. Unfortunately, we were unable to locate a good source for the broadband complex refractive index properties needed to model it.

Potassium Bromide (KBr)

KBr has a wide bandwidth and has similar performance to CsBr. The steady state temperature using our model at the Sun's surface is 805 K for a flat plate design with 1 cm of KBr on one side and a high emissivity coating on the other side. Like CsBr, increasing the shield thickness to 7 cm matches its steady state temperature of 679 K. It has a higher melting point than CsBr, potentially making it more attractive. Like CsBr, it is highly soluble in water and appears to be similarly hazardous.

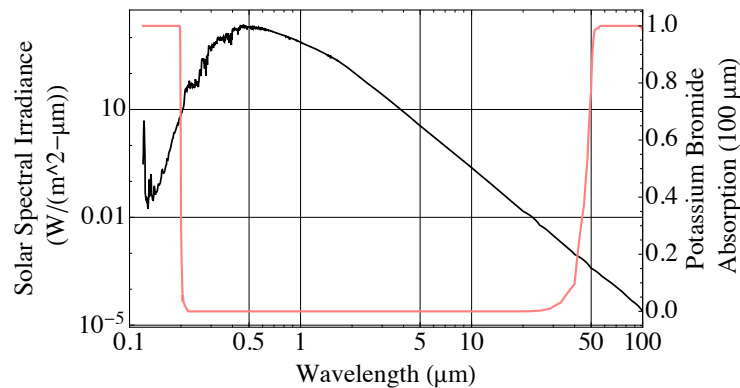


Figure I-7. The absorption curve for a 100-micron thick window of KBr plotted against the Sun's spectral irradiance.

Cesium Chloride (CsCl)

Cesium Chloride has a broad transmission band, but is extremely hygroscopic and disintegrates at ambient conditions. It does have very low solubility in other liquids, like acetone, which would allow storage. However, the extremely high water solubility makes it less attractive in our application as it would need to be sealed and protected from the damp Florida weather to keep it from deteriorating. We were unable to locate a good source for the broadband complex refractive index properties needed to model it. It has low toxicity to people and animals.

Potassium Chloride (KCl)

KCl has a broad transmission band with little UV absorption. The steady state temperature using our model at the Sun's surface is 826 K for a flat plate design with 1 cm of KCl on one side and a high emissivity coating on the other side. Increasing the thickness of KCl to 7 cm on the shield results in almost a 100 K reduction in the steady state temperature (730 K). Like the other chlorides in the table it is highly soluble in water. It is a minor irritant in small quantities, but can be toxic if ingested in large quantities - causing cardiac arrest.

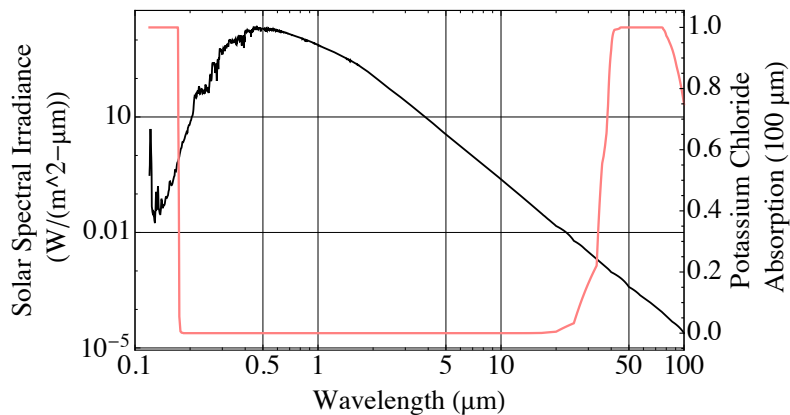


Figure I-8. The absorption curve for a 100-micron thick window of KCl plotted against the Sun's spectral irradiance.

Sodium Chloride (NaCl)

Sodium Chloride has a broad transmission band with low UV absorption. The steady state temperature using our model at the Sun's surface is 838 K for a flat plate design with 1 cm of NaCl on one side and a high emissivity coating on the other side. Increasing the thickness to 7 cm will result in a 50 K reduction in the steady state temperature (788 K). These temperatures are slightly higher than KCl due to its slightly shorter transmission cutoff in the IR. It is abundant, inexpensive, and safe but has high water solubility. Its melting point of 1074 K may make it a poor candidate for approaching the surface of the Sun.

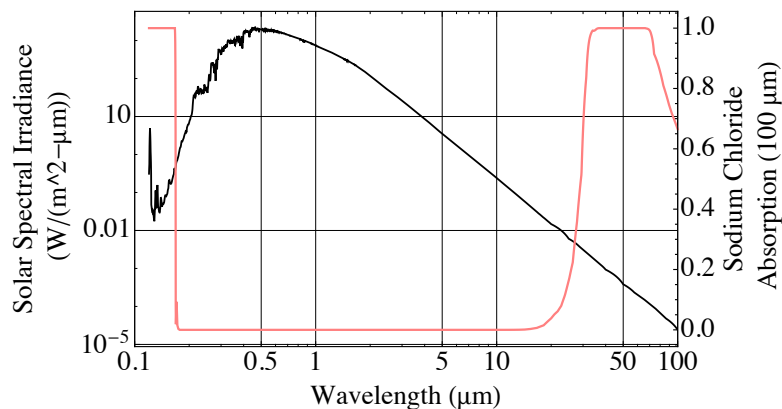


Figure I-9. The absorption curve for a 100-micron thick window of NaCl plotted against the Sun's spectral irradiance.

Rubidium Chloride (RbCl)

Rubidium Chloride has a broad transmission band, similar to CsCl but is less soluble in water and has a higher melting point. We were unable to locate a good source for the broadband complex refractive index properties needed to model it. It is a minor irritant.

Cesium Iodide (CsI)

Cesium Iodide has a very broad transmission band as seen in the absorption plot below. It also has a high index of refraction compared to the other materials. Unfortunately, the higher UV absorption pushes the steady state temperature computed by our model above the melting point of Cesium Iodide when approaching the Sun’s surface. However, this material might be worth revisiting for cryogenic applications.

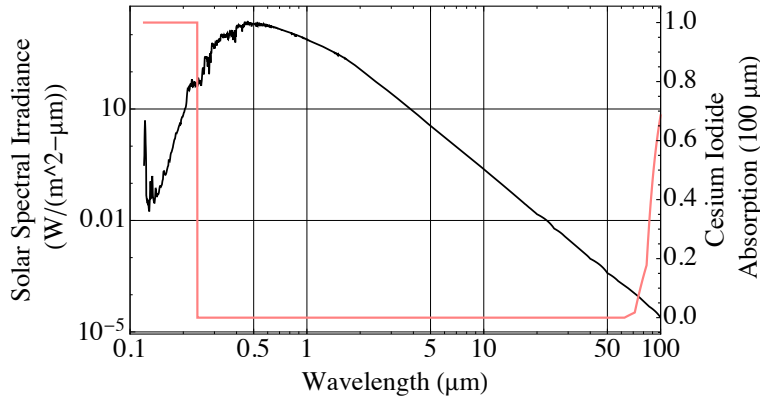


Figure I-10. The absorption curve for a 100-micron thick window of CsI plotted against the Sun’s spectral irradiance.

Aluminum Oxide (Al₂O₃)

Aluminum oxide has a shorter passband than the other materials, only extending to 7μm. However, it has a much higher melting point and can tolerate higher temperatures (2345 K) without deteriorating. The steady state temperature using our model at the Sun’s surface is 1409 K for a flat plate design with 1 cm of Al₂O₃ on one side and a high emissivity coating on the other side. Due to the higher temperatures involved, tantalum was used as the long-wave reflecting material instead of silver, as it has a much higher melting point. Increasing the thickness to 7 cm results in a 14 K reduction in the steady state temperature (1395 K). It is widely available, inexpensive (\$100 per kg) insoluble in water, and relatively safe to work with but can cause minor skin irritation.

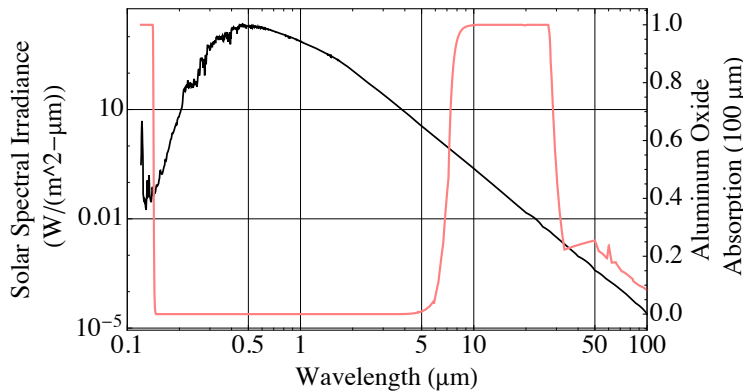


Figure I-11. The absorption curve for a 100-micron thick window of Al₂O₃ plotted against the Sun’s spectral irradiance.

Yttrium Oxide (Y₂O₃)

Yttrium oxide has a decent passband, extending to 10μm. It has a high melting point and can tolerate high temperatures (2698 K) without deteriorating. The steady state temperature using our model at the Sun’s surface is 1284 K for a flat plate design with 1 mm of Y₂O₃ on one side and a high emissivity coating on the other side. Due to the higher temperatures involved, tantalum was used as the long-wave reflecting material instead of silver, as it has a

much higher melting point. Thicker coatings of 1 cm lower the steady state temperature to 1213 K. It is available in high purity form for around \$130 for 100 g. It is insoluble in water, and considered not hazardous.

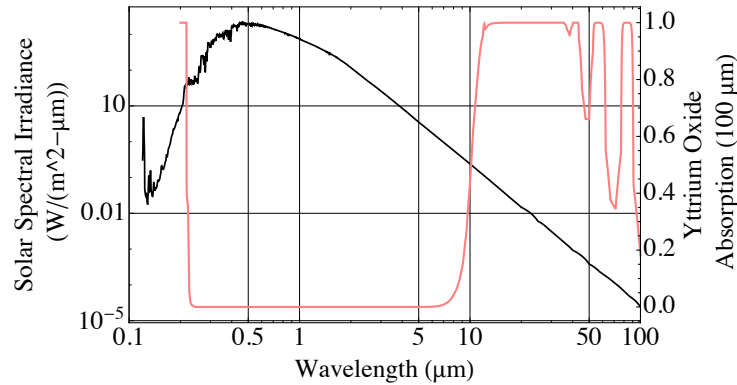


Figure I-12. The absorption curve for a 100-micron thick window of Y_2O_3 plotted against the Sun's spectral irradiance.

Hafnium Oxide (HfO₂)

Hafnium oxide has a decent passband, extending to around 14 μm . It has a high melting point and can tolerate high temperatures (3031 K) without deteriorating. The steady state temperature using our model at the Sun's surface is 2255 K for a flat plate design with 110 μm of HfO₂ on one side and a high emissivity coating on the other side. Due to the higher temperatures involved, tantalum was used as the long-wave reflecting material instead of silver, due to its much higher melting point. It is insoluble in water, and considered not hazardous. The complex refractive index was not easily found for the entire UV-IR band, so a mathematical model was used based on the paper by T. J. Bright et. al. "Optical properties of HfO₂ thin films deposited by magnetron sputtering: From the visible to the far-infrared" (<http://www.sciencedirect.com/science/article/pii/S0040609012008863?via%3Dihub>). The n and k values are shown below along with the corresponding absorption plot. The problem with the math model is that the functions transition gradually between absorption and transmission allowing much more of the Sun's spectrum to be absorbed than would likely occur in reality. Artificially forcing the value of k to 0 for wavelengths below 14 μm drops the steady state temperature to 1561 K for 110 μm of HfO₂, but it drops substantially to 855 K for 1 cm of material.

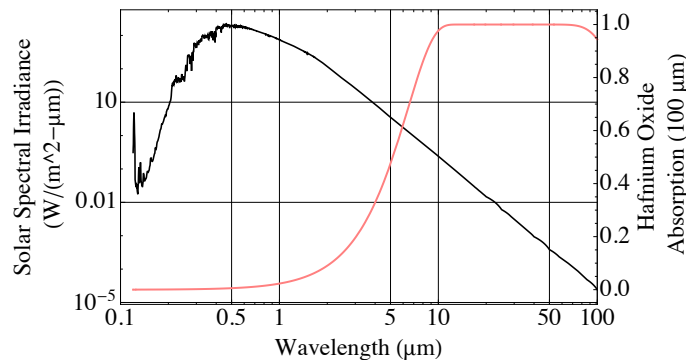


Figure I-12. The absorption curve for a 100-micron thick window of HfO_2 plotted against the Sun's spectral irradiance and the complex index of refraction as predicted from a math model.

Chemical Vapor Deposition (CVD) Diamond

Diamond is transparent from 225 nm into the far-infrared, but has some minor absorption bands between 2.5-6.5 μm due to two-phonon absorption. It is also insoluble, won't melt unless under high pressures, has a high index of refraction and CVD methods are well established to control the material properties (i.e., impurities). The steady state temperature using our model at the Sun's surface is 1602 K for a flat plate design with 100 μm of diamond on one side and a high emissivity coating on the other side. In this simulation, tantalum was used in place of silver behind the scattering layer due to its much higher melting point. This all combines to make it attractive for the solar surfing application.

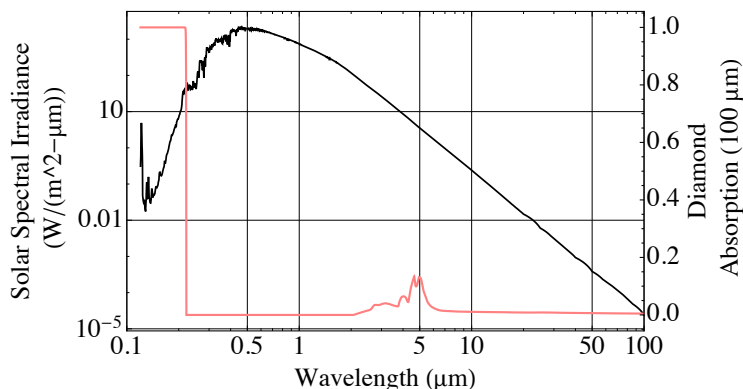


Figure I-13. The absorption curve for a 100-micron thick window of diamond plotted against the Sun’s spectral irradiance.

Summary

Table 1 below contains a summary of materials we have found with the potential for use in solar surfing along with relevant performance parameters. Out of the materials reviewed, the synthetic diamond appears to have the best temperature characteristics to approach the Sun’s surface. The computed state temperature at the Sun’s surface is still over 2000 K below its melting point. Only a very thin 100-200 μm layer is needed on top of a long wave reflecting surface like tantalum. Whereas many of the other materials require a centimeter or more of material to approach the Sun. It appears that CVD can be used to create the correct size particles needed for our scattering layer, but it’s not clear it can be used to make multiple layers with while maintaining the proper particle size. Fabrication will be the focus of future work. Several companies that make CVD diamond coatings and are involved in related research are <https://www.sp3diamondtech.com/capabilities/technology/>, <http://crystallume.com/sbirsttr-awards/>, and <http://www.diamond-materials.com/EN/index.htm>.

Material Name	Transmission Band (μm)	Melting Point (K)	1 cm Coating Sun Surface Temp. (K)	7 cm Coating Sun Surface Temp. (K)	Refractive Index @633 nm	Water Solubility @ 25°C
Barium Fluoride	0.14-14	1659	935	924	1.47	0.16 g/100 g
Calcium Fluoride	0.125-10.5	1691	1144	1113	1.43	0.0016 g/ 100 g
Lanthanum Fluoride	0.2-11	1766	**NA	**NA	1.6	insoluble
Cadmium Fluoride	0.13-12	1380	**NA	**NA	1.56	4.4 g/100 g
Sodium Fluoride	0.13-13	1269	1023	1048	1.32	4.13 g/100 g
Strontium Fluoride	0.13-18	1750	983	979	1.44	0.039 g/100 g
Cesium Bromide	0.24-40	909	792	679	1.69	123 g/100 g
Potassium Bromide	0.21-33	1003	805	679	1.56	67.8 g/ 100 g
Sodium Bromide	0.2-24	1020	**NA	**NA	1.64	94.6 g/100 g
Cesium Chloride	0.19-30	919	**NA	**NA	1.64	191 g/100 g
Rubidium Chloride	0.2-35	997	**NA	**NA	1.49	93.9 g/100 g
Potassium Chloride	0.18-25	1049	826	730	1.49	34.7g 100 g
Sodium Chloride	0.18-20	1074	838	788	1.54	36 g/100 g
Cesium Iodide	0.25-55	900	1095	1061	1.78	84.8 g/100 g
Aluminum Oxide	0.15-7	2345	1409	1395	1.76	insoluble
Yttrium Oxide	0.2-10	2698	1213	**NA	1.90	insoluble
Hafnium Oxide	0.1-14	3031	855	**NA	1.91	insoluble

CVD Diamond	.2-500	>4000	*1602	**NA	2.41	insoluble
-------------	--------	-------	-------	------	------	-----------

Table 1 – List of candidate materials with a transmission band of at least 0.25-10 μm . Aluminum Oxide was added due to its high melting point, even though its transmission band turns off at around 7 μm .
 *CVD Diamond thickness: 100 μm **NA = Not Analyzed

Figure I-14 shows a summary chart comparing the melting point to the steady state temperature at the Sun’s surface as determined by our model. The Sun side is coated with the scattering material (about 1 cm) over a layer of silver (tantalum for oxides and CVD Diamond). The backing is assumed to be made from a high emissivity material ($\epsilon=0.9$). Diamond is the exception with a 100 μm thick coating.

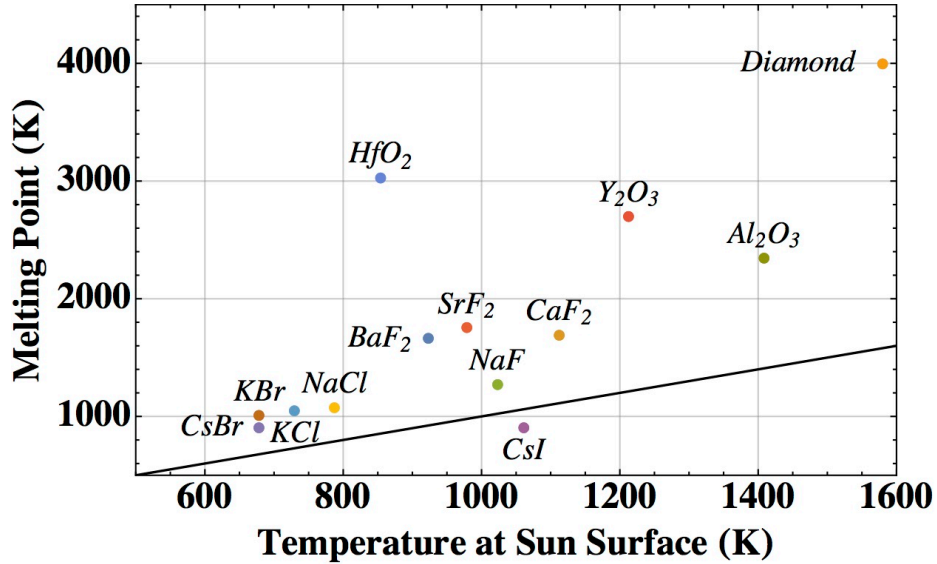


Figure I-14. Plot comparing the performance of different scattering materials at the Sun’s surface with a 1 cm thick coating. Diamond is the exception with a 100 μm thick coating.

8. APPENDIX II- A REPORT ON DETECTING AND REMOVING WATER FROM RIGID BaF_2 SAMPLES.

This report was written under contract to the KSC Engineering Services Contract (ESC).
Authors/contributors: Dr. Tracy Gibson, Jerry W. Buhrow, Jan M. Surma, Robert B. Cox, and Johnny L. Kerce.

8.1 Introduction

Over the past several years the National Aeronautics and Space Administration (NASA) Kennedy Space Center (KSC), NASA Innovative Advanced Concepts (NIAC), and NASA Launch Services Program (LSP) have funded a project to demonstrate the feasibility of developing a rigid cryogenic selective surface based on a rigid diffusive surface. NASA, with the support of ESC chemists and technicians, explored multiple approaches for creating the selective surface, including sintering and producing a sol-gel. The ESC chemists fabricated multiple coating samples and evaluated them under a scanning electron microscope (SEM) and X-ray photoelectron spectroscopy (XPS) to obtain the diffusive layer's physical characteristics. SEM images were also acquired of starting materials to serve as a baseline. The coating samples were optically tested in the KSC Applied Physics Laboratory (APL) at room temperature and then the samples with acceptable results were tested in a cryo-cooler setup, which simulated a deep space environment (vacuum with a very cold background). Testing was performed in an iterative process where coatings were fabricated and tested, and feedback was used to generate an improved next-generation coating. One of the overarching questions that still remains to be answered is to whether the rigid coating samples contain occluded water, which could be an issue in deep-space applications. This report will describe the methods used to determine if the samples contain occluded water and if that water can be removed using either dry gas flow or vacuum.

8.2 Sample Preparation

Multiple approaches were utilized in the preparation of the materials required for fabrication of rigid test specimens. A general room-temperature synthetic method was developed based on the work by Wu.¹ In a flask, stirred using a mechanical mixer, was placed 400 ml of 0.3 M $Ba(NO_3)_2$ solution. This solution was stirred at 500 RPM using a mechanical mixer. While mixing, 400 ml of 1.0 M NH_4F solution was added and the stirring rate was increased to 750 RPM. A white solid formed almost immediately upon the addition of the NH_4F solution. The mixture was stirred an additional 1 minute to ensure the reaction was completed. The solids were then collected using centrifugation (5 minutes at 5000 RPM). The collected solids were washed 3 times with 25 ml of nanopure water and dried using freeze drying. This approach was modified several times in an attempt to get the “perfect” BaF_2 crystal size. Modifications included changing the reaction temperature, changing the concentration of reactants, and changing the mixing method. Each method produced a different size of BaF_2 nanocrystals but

none were the exact size desired. The method with a lower concentration of reactants was identified as the best method to date.

Once a sufficient mass of BaF₂ nanocrystals were produced, rigid test specimens were prepared using a pressing/sintering method. A known mass of barium fluoride was added to a weighing boat and the appropriate mass of nanopure water was added. The mixture was stirred to remove any large lumps. Once mixed, the mixture was placed into a ceramic mold and pressed using a Carver press. Once pressed, the samples, still in the ceramic molds, were placed in a Carbolite CWF 1300 Box Furnace equipped with an exhaust vent and sintered using the sintering profile shown in Table 1.

Table 1. Sintering Conditions for Powder Sintering.

Temperature Profile	Comment
Ramp from RT – 250 °C	Hold at 250 °C for 10 minutes
Ramp from 250 °C – 500 °C	Hold at 500 °C for 10 minutes
Ramp from 500 °C – 750 °C	Hold at 750 °C for 10 minutes
Ramp from 750 °C – 780 °C	Hold at 780 °C for 60 minutes
Power off Furnace	Allow to cool to RT overnight

8.3 Water Removal and Detection Methods

Multiple methods were utilized in an attempt to remove occluded water from the rigid BaF₂ test specimens. These methods included heating under dry-gas flow, dry-gas flow at room temperature, and vacuum water removal. In the case of the heating under dry-gas flow, a small sample of sintered BaF₂ (~ 20 mg) was placed in a thermogravimetric analyzer (TGA, Figure 1) and heated at 5°C/minute from room temperature to 500°C under dry nitrogen flow. The mass of the sample is monitored versus time and temperature. In the case of dry-gas flow at room temperature, a rigid, sintered BaF₂ test specimen was placed on a balance inside a chamber and dry air was flowed into the chamber to reduce the humidity (Figure 2). The change in mass was monitored versus time. In the case of vacuum water removal, a rigid, sintered BaF₂ test specimen was placed inside a vacuum-safe container and the mass was recorded (Figure 3). The container holding the BaF₂ sample was then placed under vacuum for 5 minutes, after which time the container was sealed and a new weight was obtained. The pressure was then released and the mass was monitored versus time.

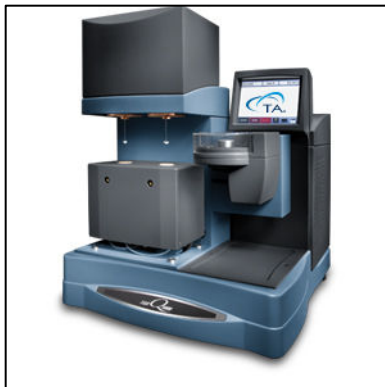


Figure 1. TA Instruments Q-5000 TGA.



Figure 2. Dry-Gas Flow Setup (Room Temperature).



Figure 3. Vacuum Water Removal Hardware.

8.4 Other Water Removal Detection Methods

Additional methods (other than mass change) were used to determine if water could be removed from a rigid, sintered BaF_2 test specimen. These methods were scanning electron microscopy/energy-dispersive X-ray spectroscopy (SEM/EDS) and x-ray photoelectron spectroscopy (XPS). SEM/EDS has the ability to determine chemical composition of materials in an ultra-high vacuum environment; SEM/EDS does not provide chemical structure, only composition. Kaya et al. described the use of XPS to study the structure of thin-film water on a BaF_2 surface² and reported that they were able to differentiate between occluded water and hydroxide ion, which is a possible impurity. Barraclough et al. studied the adsorption of water vapor on a variety of fluoride compounds, including BaF_2 ,³ and stated that water adsorption on the BaF_2 surface is solely a physisorption process and that the water can be removed via vacuum at room temperature.

8.5 Results

TGA data indicated that water could be removed from a rigid, sintered BaF_2 test specimen by heating in a dry-gas environment (Figure 4). Data indicates that water removal was initiated as soon as the sample heating started and continued until approximately 246 °C, where any water that was remaining in the sample was removed. A total mass loss of approximately 0.093% was recorded and is thought to be the amount of water removed from the sample. However, the data collection started at a value greater than 100% so the exact weight loss isn't clear. The sudden weight loss at 246 °C of 0.054% is attributed solely to water loss. An isothermal test conducted using TGA was not a success; the data was not clear and it was difficult to determine the extent of water removal.

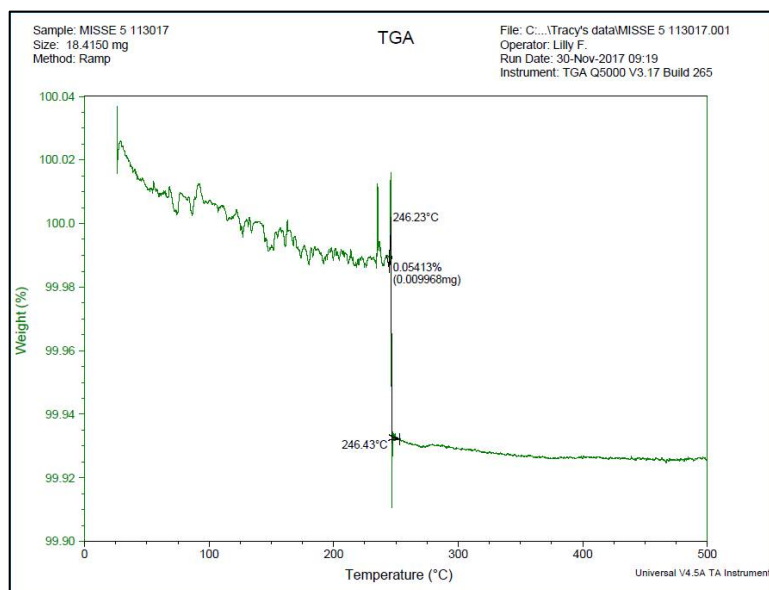


Figure 4. TGA Data for a Rigid, Sintered BaF_2 test specimen.

The dry-gas flow removal method did not prove to be successful. Initially, the test specimen appeared to lose mass (which was believed to be water removal). However, after several hours, the mass started to increase and continued to increase for the remainder of the test; the mass increased in the test specimen even though the relative humidity inside the chamber dropped to 1%! The mass gain could not be explained and a repeat of the test is planned for the near future.

The vacuum water removal method was somewhat successful but still has some unknowns. A test specimen was placed under vacuum using a scroll pump for 5 minutes, after which time it lost approximately 0.019 grams (0.064%). This loss of 0.064% is similar in magnitude to the loss found using TGA (~0.093%).

The SEM/EDS data on an aliquot of synthesized BaF_2 nanocrystals did not show the presence of oxygen or water. This is an important finding in that there was no evidence of occluded water in these high-surface area particles (higher surface area than the rigid, sintered test specimens). However, it should be noted that SEM/EDS has a relatively high detection limit for oxygen, and therefore, water. Water may still be present but at a level below the detection limit.

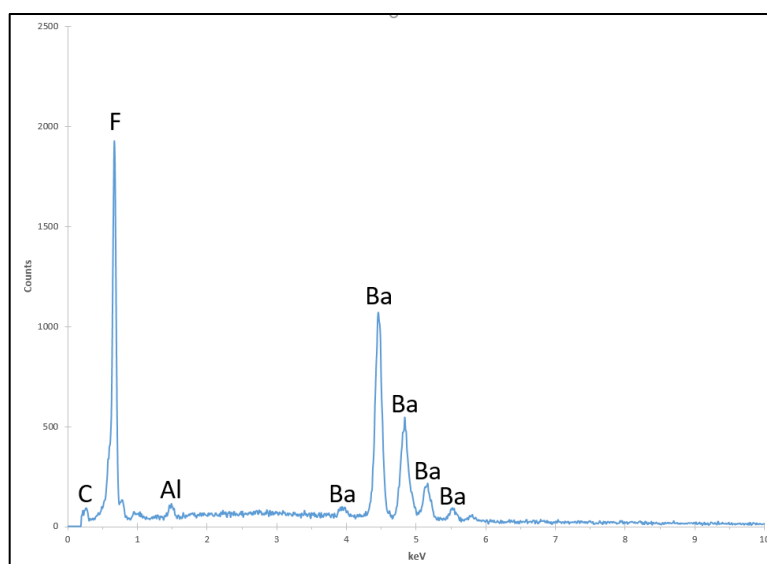


Figure 5. SEM/EDS Spectrum of Synthesized BaF_2 Nanocrystals.

The XPS data did not provide clear evidence that occluded water could be removed via ultra-high vacuum (which is the conditions for XPS). The XPS spectrum clearly showed the presence of barium and fluoride but also showed the presence of calcium and oxygen (Figure 6 and Table 2). Based on this data it is not clear if the oxygen is present as water or an impurity associated with the calcium. The source of calcium is unknown but may be attributed to the ceramic mold that was used to fabricate the rigid, sintered BaF_2 test specimen. Experiments will be conducted using the opposite side of the test specimen which did not contact the ceramic mold to determine if the source of the calcium is the ceramic mold.

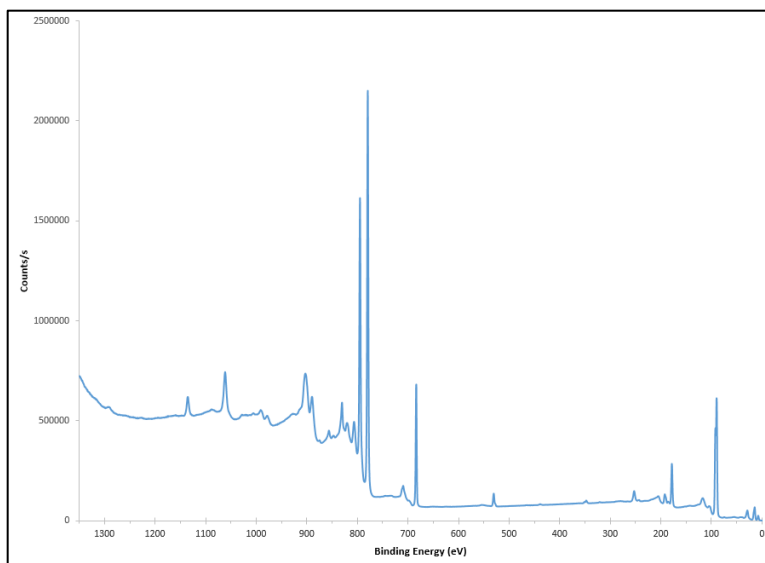


Figure 6. XPS Spectrum of a Rigid, Sintered BaF₂ Test Specimen.

Table 2. Peak Table for XPS Spectrum of BaF₂ Test Specimen.

Element	Peak	Binding Energy (eV)	Atomic %
Oxygen	O1s	530.5	10.19
Fluorine	F1s	683.7	57.26
Barium	Ba3d _{3/2}	795.0	31.06
	Ba3d _{5/2}	779.7	
	Ba4d	89.0	
Calcium	Ca2p	347.0	1.49

8.6 Conclusions

Understanding the water content and removal of occluded water from rigid, sintered BaF₂ samples is a longstanding topic that needs to be addressed before one can fully understand the viability of using these materials in deep-space applications. For deep space application, it is desirable that if there is occluded water present that this water be removable using vacuum (which is readily available in space). Multiple experiments were conducted in an attempt to determine if occluded water was present in the rigid, sintered BaF₂ test specimens and if so, could the water be removed. Firstly, most, if not all, of the experiments conducted showed that there was water present in the rigid, sintered test specimens. However, it is not clear in all cases that the water can be removed easily. Experiments conducted using vacuum and ultra-high vacuum to remove the occluded water were inconclusive and will need to be repeated, although it was shown that the test specimens lose mass upon evacuation; however, at this point, we cannot confirm that the mass loss is due to water loss. Dry-gas removal methods also proved to be inconclusive due to instrumentation issues. As far as occluded water removal in general, it is clear from the TGA data that occluded water can be removed by heating to approximately 260 °C. While successful, this is not the preferred method for occluded water removal for deep-space applications.

8.7 References

1. Wu, D.; Wu, X. Lv, Y.; Wang, H. *Materials Letters* **2008**, *62*, 3003-3006.
2. Kaya, S.; Schlesinger, D.; Yamamoto, S.; Newberg, J.T.; Bluhm, H.; Ogasawara, H.; Kendelewicz, T.; Brown, G.E., Jr.; Pettersson, L.G.M.; Nilsson, A. *Sci. Rep.* **2013**, *3*, 1074.
3. Barraclough, P.B.; Hall, P.G. *J. Chem. Soc. Faraday Trans. 1* **1975**, *71*, 2266-2276.